# Charles University
# Faculty of Science

Modeling of Chemical Properties of Nano- and Biostructures

**Priyam Bharadwaz**

# Chemical reactivity through the lens of traditional and non-traditional concepts

**Doctoral thesis**

Supervisor: **RNDr. Martin Srnec, PhD.**
Advisor: **prof. Mgr. Lubomír Rulíšek, DSc.**

Prague 2024

## Declaration of the author:

I declare that I carried out this doctoral thesis independently, and only with the cited sources, literature and other professional sources.

I understand that my work relates to the rights and obligations under the Act No. 121/2000 Sb., the Copyright Act, as amended, in particular the fact that the Charles University in Prague has the right to conclude a license agreement on the use of this work as a school work pursuant to Section 60 subsection 1 of the Copyright Act.

Date & Place Signature

## Acknowledgements

At first, I would like to express my sincere gratitude to my supervisor Dr. Martin Srnec for his constant support, guidance, help, motivation and fruitful advice during the entire duration of my doctoral studies. I would also like to gratefully acknowledge my lab member Mauricio Maldonado Dominguez for his help, scientific inputs and our discussions related to my research work. My thanks go to Zuzana, Stepan, Jakub, Santi, Tom, Mehrnoosh, Payman, Mahesh for their kind support.

Last but not least, all of these would not have been possible without love, care and support from my mother, my younger sister and my family and friends. Finally, I would like to thank my loved ones, friends who always stood by me with constant support, encouragement and motivation that allowed me to finish this thesis. Thank you for putting your belief and faith in me.

# Abstract (EN)

The common theme of the thesis is the understanding of chemical reactivity in the field of bioinorganic and (bio)organic chemistry from the perspective of traditional transition state theory (TST) as well as approaches going beyond. Specifically, I present two studies in this thesis – one focused on reactivity factors shaping methanogenesis mostly using TST and one exemplifying a non-TST case in chemical reactivity, which I solved using a new tool that I co-develop during my PhD studies.

For the first thesis project based on TST, we took on the task of understanding catalytic efficiency of the F430 coenzyme in methanogenesis as compared to its four bio-synthetic precursors, providing a plausible view of how the evolutionary driving force shapes the biocatalytic proficiency of F430 towards $CH_4$ formation. In nature, production of methane is facilitated by a key enzyme known as methyl coenzyme M reductase (MCR). MCR catalyzes the final step in the conversion of coenzymes M ($H_3C{-}SCoM$) and B ($CoBS{-}H$) to methane and heterodisulfidic product. The active site of the enzyme hosts an Ni-containing cofactor F430. The catalytic mechanism can be then explained as F430-mediated reductive cleavage of the $H_3C{-}S$ bond in coenzyme M, yielding a transient $CH_3$ radical capable of extracting a hydrogen atom from the S−H bond of coenzyme B. Despite this, the key reactivity factor contributing to catalytic efficiency of MCR is still in its nascent phase. In this work, I am trying to understand the driving force behind the methanogenesis. I performed computational investigation to explore whether and why F430 is unique for methanogenesis in comparison to four identified precursors formed consecutively during its biosynthesis. Indeed, I obtained the native F430 cofactor as most competent for methane bioproduction compared to all precursors. In fact, there is a sequential improvement of catalytic efficiency at each enzymatic step towards F430 maturation. Unexpectedly, the native F430 cofactor possesses the highest reduction potential, which suggests that F430 would be the least proficient reductant for the cleavage of the $S{-}CH_3$ bond of coenzyme M. I found out that a key contributing factor that dominates the reactivity for reductive cleavage of the $S{-}CH_3$ bond is actually the formation of Ni–S bond. The native F430 appeared as the weakest electron donor along the series and consequently, possessed the most covalent Ni–S bond and hence the most stable rate-determining transition state leading to the highest reaction rate.

In the second part of this thesis, I explore reactions for which TST is inappropriate method of understanding their chemical reactivity. According to TST, transition state is the highest-energy, short-lived state along the minimum energy pathway that the reactants must have to overcome to form the products. These types of reactions can be described within the TST framework because a major product is determined by the lowest energy barrier. However, in addition to these reactions, there is now an increasing number of reactions in which a single transition state may be responsible for the formation of multiple intermediates or products simultaneously. These types of reactions are known as multi-furcating reactions. Bifurcating reactions produce two distinct products channels originating from a solitary transition state. Therefore, they represent paradigmatic examples that defy explanation within TST. Therefore, with the increasing amount and importance of these reactions in both organic and bioinorganic chemistry, there is a growing demand for a suitable theoretical tool that can precisely quantify the outcome of products at a minimal cost. Till date, there are only a few computational methods that are reported for prediction and quantification of the product outcome for such reactions. In this thesis, I computationally proposed a simple approach that satisfies these criteria, by evaluating the energy distribution within the reactive mode of the key transition state. This method was first introduced by our group and relies on the kinetic energy distribution (KED) within the reactive mode of the key transition state. Our KED-calculated product selectivity within the reactive mode yields an excellent agreement with experimentally reported product ratios and predicts the correct selectivity for 89% of studied cases. I consider 60 different types of bifurcating reactions, which includes pericyclic reactions, rearrangements, fragmentations and metal-catalyzed processes as well as a few trifurcating reactions. Given its predictive power, the procedure makes reaction design feasible even in the presence of complex non-TST chemical steps.

Later, I also extended the application of KED analysis in studying the nature of generated transient methyl-radical in the first catalytic step of methane production by methyl coenzyme M reductase. KED analysis reveals that kinetic energy in the reactive mode is concentrated in the motion of the nascent methyl radical.

# Abstrakt (CZ)

Cílem diplomové práce je pochopení chemické reaktivity ve vybraných oblastech bioanorganické a (bio)organické chemie a to s použitím tradiční teorie tranzitního stavu (TTS), tak i přístupů jdoucích za tuto teorii. Konkrétně v této práci uvádím dvě studie – jednu, která se opírá převážně o TTS při řešení faktorů řídící metanogenezi a jednu ilustrující chemický případ, který nelze řešit v rámci TTS a pro jehož pochopení jsem použila teorerický nástroj, na jehož vývoji jsem se podílela.

Cílem mého prvního projektu bylo porozumět katalytické schopnosti koenzymu F430 při tvorbě metanu s důrazem na jeho srovnání se čtyřmi biosyntetickými prekurzory a to za účelem získání věrohodného pohledu na evoluční hnací sílu, jež utváří biokatalytickou způsobilost F430 směrem k tvorbě $CH_4$. V přírodě je produkce metanu usnadněna klíčovým enzymem metyl-koenzym M reduktázou (MCR). MCR katalyzuje reakci mezi koenzymy M a B ($H_3C$–SCoM a CoBS–H) vedoucí na metan a heterodisulfidický produkt. Aktivní místo tohoto enzymu hostí kofaktor F430, v jehož středu se nachází redoxně aktivní ion niklu. Ústřední částí reakčního mechanismu je pak redukční štěpení vazby $H_3C$–S v koenzymu M zprostředkované ionem niklu a uvolňující metylový radikál, jenž v následujícím kroku stěpí vazbu S–H v koenzymu B za vzniku metanu. Navzdory všeobecné shodě ohledně reakčního mechanismu zůstává otázkou, jaké reakční faktory rozhodují a vysoké katalytické účinnosti MCR. Abych prozkoumala, zda a proč je F430 jedinečně účinný katalyzátor, srovnala jsem jeho reakční vlastnosti s vlastnostmi čtyř jeho prekurzorů, které se tvoří coby stabilní intermediáty během jeho biosyntézy. Výpočty ukazují, že kofaktor F430 je skutečně nejefektivnější, přičemž dochází k postupnému zlepšování katalytické účinnosti v každém biosyntetickém kroku směrem k F430. Překvapujícím momentem je fakt, že kofaktor F430 má nejvyšší redukční potenciál. To odporuje očekávání, že F430 působí jako nejsilnější reduktant, a tedy umožňuje nejsnažší redukční stěpení vazby S–$CH_3$ v koenzymu M. Klíčovým faktorem, který řídí redukční štěpení vazby S–$CH_3$ je naopak tvorba vazby Ni–S. V tomto ohledu jsem zjistila, že nativní F430 tvoří nejkovalentnější vazbu Ni–S, což stabilizuje tranzitní stav vedoucí k nejvyšší reakční rychlosti mezi studovanými systémy.

Ve druhé části této práce předkládám studium reakcí, které nelze zkoumat pomocí standardní TTS. Podle TTS je tranzitní stav stavem s nejvyšší energií podél reakční koordináty (jednoho reakčního

kroku). Srovnají-li se dva reakční cesty (vedoucí ke stejnému produktu, či dvěma odlišným produktům), z nichž jedna má níže položený tranzitní stav, pak tato cesta bude tou, po které se reakce vydá. Tyto typy reakcí lze popsat v rámci TTS. Kromě těchto reakcí jsou i takové reakce, které vykazují jeden tranzitní stav pro dvě různé reakční cesty vedoucí ke dvěma různým produktům. Tyto typy reakcí jsou známé jako bifurkační reakce a jsou zářnými příklady, které se vymykají vysvětlení v rámci TTS. S rostoucím množstvím a významem těchto reakcí v organické i bioanorganické chemii roste poptávka po vhodném teoretickém nástroji, který dokáže přesně a přitom levně kvantifikovat poměrné zastoupení produktů. Dosud existuje pouze několik výpočetních metod, které byly použity k predikci a kvantifikaci takového poměrného zastoupení. V této práci jsem navrhla jednoduchý přístup, který kvantifikuje poměrné zastoupení produktů pomocí analýzy distribuce kinetické energie v reaktivním módu tranzitního stavu (anglicky kinetic energy distribution - KED). Selektivita produktu vypočítaná na základě analýzy KED v reaktivním módu poskytuje vynikající shodu s dostupnými experimentálními daty, přičemž správná selektivita je předpovězená pro 89 % ze 60 studovaných případů.

## Contents:

## 1. Introduction and objectives:

In the intricate realm of chemical kinetics, conventional transition state theory (TST) stands as a venerable cornerstone, providing a profound understanding of the fundamental processes governing chemical reactions. Developed in the mid-20th century, by the collaborative efforts of towering figures such as Eyring, Polanyi, and Wigner, TST provides a conceptual framework to understand the dynamics of reactions.[1-4] Central to TST is the concept of an energy barrier that reacting molecules must have to overcome to reach the transition state and proceed to the product formation. The foundation of TST relies on the notion of a transition state—a fleeting, quasi-stationary point along the reaction coordinate. It recognizes that reactions take place in a series of intermediate steps, with the transition states serving as pivotal points where the reacting system undergoes a critical transformation. This theory elegantly connects the reaction rates with the energetics associated with molecular intricacies of bond-breaking and bond-forming processes. By considering the statistical distribution of molecular energies and the geometry of the transition state, TST provides a quantitative framework for predicting reaction rates and understanding the factors influencing reaction dynamics. [5-6]

The success of TST can be documented by many and diverse examples from literature. In the realm of bio-inorganic chemistry, TST aids in unraveling the catalytic mechanisms of metalloenzymes, exemplified by the analysis of cytochrome P450's oxidative reactions.[7] Shifting focus to bio-organic chemistry, TST elucidates enzymatic catalysis and molecular recognition, as for example seen in the case of chymotrypsin's peptide bond cleavage.[8-9] Exploring the green landscapes of photosynthesis, TST also applies to decode the activation barriers within the oxygen-evolving complex (OEC) of photosystem II.[10-11] Further, TST unveils the nuances of DNA replication, exemplified by its role in understanding DNA polymerase-catalyzed nucleotide incorporation.[12]

Beyond many other examples, where TST is absolutely indispensable tool for understanding reaction mechanisms and chemical reactivity in general, we also witness an increasing number of reactions that exhibit non-statistical (non-TST) behavior in nature. In such cases, the conventional TST may no longer be suitable for elucidating their behavior.[13] TST relies on several assumptions, neglecting various effects that can hold significance in certain reactions.[13] Unlike TST, which assumes a single pathway leading from reactants to products, non-TST embraces the notion of multiple concurrent pathways and explores the influence of dynamic fluctuations on reaction outcomes. Quantum tunneling and dynamic motions of reactants and intermediates are integral aspects of non-TST, acknowledging that chemical transformations are not solely dictated by the energy landscape but are also shaped by the dynamic interplay of molecular entities.[14] While TST focuses on the elusive intermediates along reaction pathways, non-TST ventures into the dynamic and complex scenarios where chemical transformations unfold without conforming to well-defined transition states. Examples of non-TST phenomena abound in chemistry, ranging from hydrogen transfer reactions at low temperatures to enzymatic processes where dynamics play a pivotal role.[15-19] Further, there are also nowadays growing number of organic reactions which also deviates from TST, known as bifurcating reactions.[20-22] Bifurcating reactions are chemical processes where a set of reactants can follow multiple distinct pathways, resulting in different products. Unlike traditional reactions with a single outcome, bifurcating reactions create branching points, offering diverse routes for the transformation of reactants into various products. Understanding these reactions is crucial for unraveling complex reaction dynamics and gaining insights into the factors that influence multiple outcomes in chemical systems.

In this thesis, I provide some insights into chemical reactivity through the lens of both traditional transition state theory (TST) and non-traditional approaches in the rich landscapes of bioinorganic and (bio)organic chemistry. This thesis encapsulates two distinct studies (later as **Project I** and **II**), each offering a glimpse into the intricate realm of chemical reactivity. The first study casts a focused lens on the underlying factors steering methanogenesis (**Project I**), employing the classical principles of TST to unravel the intricacies that govern this fundamental methanogenesis process. On the other hand, the second study diverges into uncharted territory, embracing a non-TST perspective on quantification of bifurcating product ratios (**Project II**). Notably, the latter project is navigated using a novel tool co-developed during the course of my PhD studies. A brief overview of both studies is described in the following section.

## 1.1. Project I

Methane is a potent greenhouse gas and plays a vital role in climate change. Naturally, methane production takes place via both biogenic and abiogenic processes. Biogenic sources include the decomposition of organic matter in wetlands, livestock digestion, and digestion of certain microorganisms while abiogenic sources comprise the volcanic activity and chemical reactions in the Earth's crust. Globally, about 90 to 95% of methane production takes place biologically in anoxic environments from $CO_2$, $H_2$, acetate, methylamines, and methanol by methanogenic archaea.[23-25]

The process of production of methane by microorganisms is called methanogenesis, which is mediated by consortium of methanogenic archaea under strictly anaerobic condition. The key enzyme that catalyzes the terminal and rate-determining step in biological methanogenesis is known as methyl-coenzyme M reductase (MCR). MCR is composed of dimer of three protein subunits MCRA (α), MCRB (β), and MCRG (γ), adopted an $\alpha^2\beta^2\gamma^2$ heterohexamer-type conformational arrangement.[26-27] Each of the two identical dimers hosts the catalytic active sites with a nickel-containing F430 cofactor, structurally similar to porphyrin, chlorophyll, and vitamin B12.[28-31] The coordination environment of charged carboxylate residues of F430 can be explained by hydrogen bonding and electrostatic interaction with the peptide nitrogen atoms of the protein side-chain linkage. MCR is the naturally abundant Ni-containing protein that promotes the conversion of methyl donor, methyl-coenzyme M ($CH_3$–SCoM) and electron donor, coenzyme B (CoB–SH) to methane and the mixed heterodisulfide, CoMS–SCoB product as shown in **Figure 1**. [32-33] Apart from this, MCR is also found to be capable of catalyzing the reverse reaction, as reported for anaerobic methanotrophic sulfate, nitrate, or $Fe^{III}$-reducing bacteria.[30,32-34]

The biosynthesis pathway of F430 is complex and involves several convoluted enzymatic steps.[35] The early initial stage involves the synthesis of a precursor molecule called precorrin-2. This precursor is derived from the common porphyrin biosynthesis pathway found in many organisms. After that precorrin-2 is converted to the unique sirohydrochlorin precursor, a complex cyclic tetrapyrrole moiety. Recently, Warren and co-workers elucidated that the late-stage bio-modification of F430 comprises of four enzymatically controlled steps.[35] The first step involves the transformation of sirohydrochlorin to coenzyme-F430 by insertion of a nickel atom in the center of tetrapyroole ring. After that the overall process is followed by stepwise modifications:

chelation, amidation, reduction by six electrons with addition of seven protons, lactamization, and closure of a propionate side chain coupled to water extrusion. The structure of all experimentally identified Ni-anchoring biosynthetic precursors of F430 are provided in **Figure 2**.

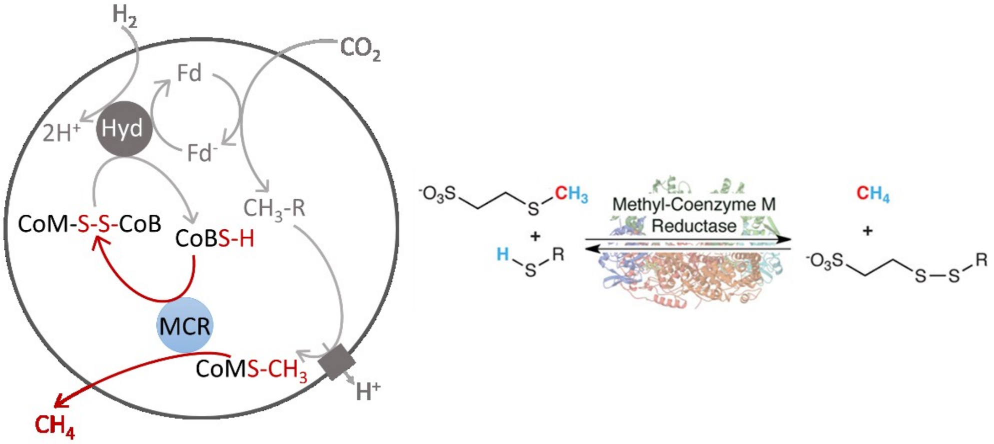

**Figure 1:** Global catalytic cycle showing the last step of methanogenesis.[36] The last and terminal step of methanogenesis is catalyzed by bio-enzyme MCR by conversion of substrates $CH_3S$–CoM and CoB–SH to products $CH_4$ and CoMS–SCoB.

To date, numerous studies have been conducted to unravel the mechanistic details of methane production by MCR.[37-45] One of the previously suggested mechanisms includes the formation of the organometallic intermediate methyl-Ni(III) supported by experimental evidence using model F430 complexes with the presence of various activated alkyl donors.[46-48] However, the formation of this type of intermediate is not actually observed in MCR in the presence of the native methyl donor co-substrate $CH_3$–SCoM. Density functional theory calculations also revealed the associated endergonicity of this pathway and therefore, ruled out the possible existence of organometallic $H_3C$–Ni(III) intermediates.[42-43,49] The MCR reaction mechanism considered in this thesis coincides with another previously formulated mechanism for which there is currently a consensus. The mechanism, initially proposed through computational efforts by Siegbahn,[44,50] gained experimental support later from Ragsdale and co-workers[51] as summarized in **Figure 3**. The catalytic cycle essentially consists of three consecutive steps: (*i*) the $H_3C$–SCoM bond undergoes reductive cleavage, releasing the transient methyl radical and leading to the oxidation of nickel center from +I to +II with the concomitant formation of a Ni–S bond between Ni$^{II}$ and SCoM; (*ii*) the H–S bond in HS–CoB undergoes an attack by the transient methyl radical, leading to the liberation of $CH_4$ and the generation of $^{\bullet}$SCoB radical; finally (*iii*) the Ni–bound SCoM couples with CoBS$^{\bullet}$ radical to generate Ni(II)–disulfide anionic radical complex.

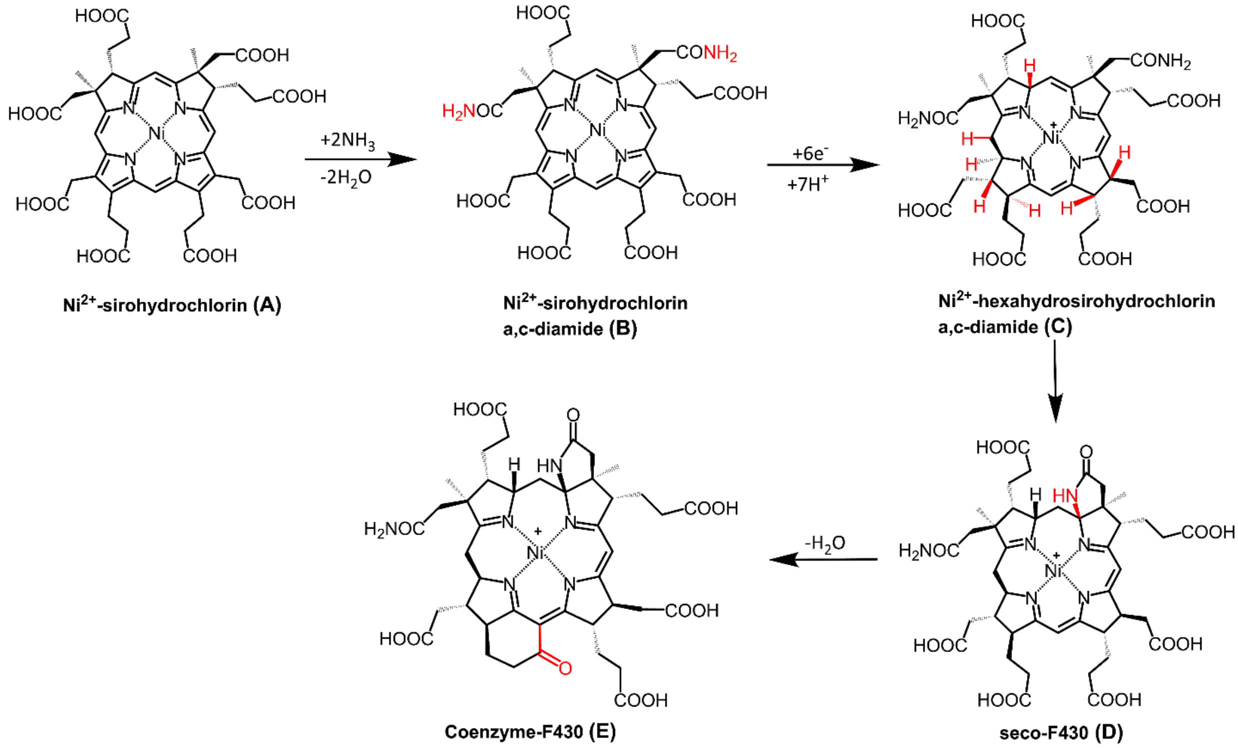

**Figure 2:** Biosynthesis of the native F430 cofactor comprises four successive Ni-containing precursors. We used labels **A**, **B**, **C**, **D** and **E** for the biosynthetic precursors and native F430 cofactor, respectively. Later, I maintained this notation throughout the whole **Project I**.

In the project on MCR, my main goal was to understand whether and why F430 is unique for methanogenesis in comparison to its four identified precursors formed consecutively during its biosynthesis and to reveal the key contributing factors that compel nature to follow such a complex and energy-demanding pathway to optimize reactivity toward methane formation (and its oxidation in the reverse process). To this aim, I computationally investigated energetics of catalyzed reaction and dissected key reactivity factors in each reaction step for the native F430 cofactor and its four biosynthetic precursors from **Figure 2** (for convenience, I use the labels **A**, **B**, **C**, **D** and **E** to refer to the four biosynthetic precursors and native F430, respectively). I continued to use this notation everywhere later. I carried out density functional theory (DFT) calculation to evaluate redox properties of **A**, **B**, **C**, **D**, **E** and correlated with the associated reaction energetics, which led to unexpected findings about the key reactivity factors. Indeed, I observed that the native cofactor **E** is the most effective catalyst. Moreover, the catalytic efficiency is improved during each subsequent step of F430 biosynthesis. I found that the key reactivity factor responsible for this trend is the Ni–S bond formation occuring during catalytic cycle. I also conducted a dedicated study to understand the nature of the transient methyl radical that is generated in the rate-determining step of the catalytic cycle. I performed the kinetic energy distribution (KED) analysis of the reactive mode in the trasition state of the rate-determining **step 1** (**Figure 3**). I showed that most of the kinetic energy in the reactive mode is accumulated in the $CH_3$ fragment and it is indeed the highest in **E**, which further contributes to the highest catalytic efficiency of the native cofactor as compared to its **A**–**D** precursors.

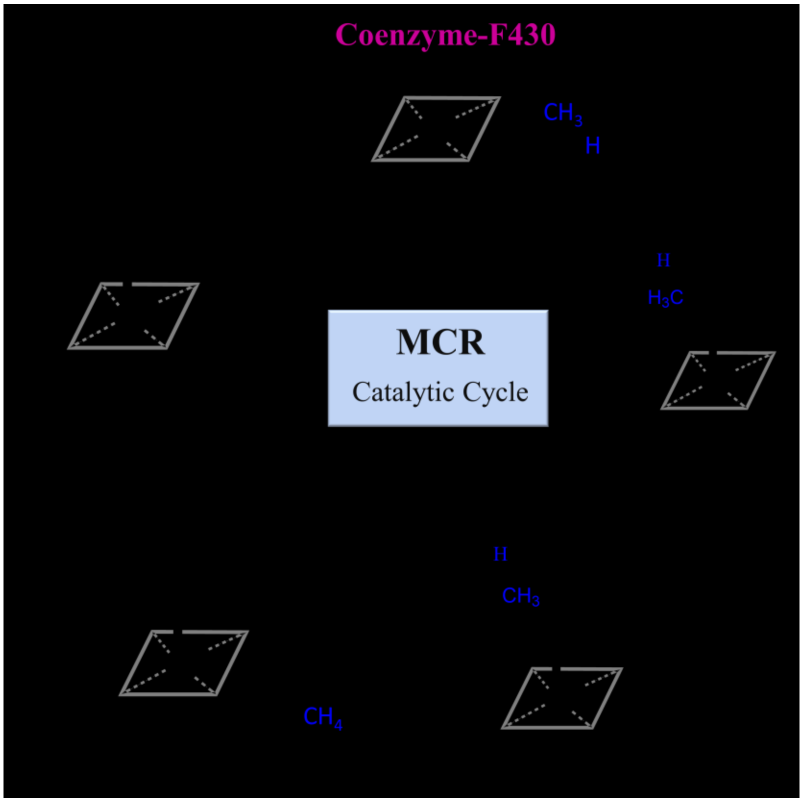

**Figure 3:** Canonical catalytic cycle of the methyl-coenzyme M reductase (MCR).

## 1.2. Project II

In the next part of this thesis, I demonstrate the adoption and application of the KED-based analysis to predict the product ratios for a range of diverse set of bifurcating reactions. This type of reaction is now increasingly in demand, but predicting accurate product selectivities is quite challenging in terms of experimental cost and time. Bifurcating reactions are archetypal examples of reactions that fall outside the scope of traditional Eyring's TST.[20-22,52-56] These reactions by nature follow one common ambimodal transition state $TS_1$, responsible for the formation of two products at the same time, once potential energy surface (PES) bifurcates after reaching valley-ridge inflection point (VRI) without the presence of any additional transition state (shown in **Scheme 1**).[57-62] Therefore, they can not be studied within the framework of TST. Here, I explore the scope of computational approach that relies on KED within the reactive mode of ambimodal $TS_1$ to quantify the product selectivities for a diverse set of furcating reactions. I use the advantage of this recently developed computational method by our group to study selectivity of these reactions, since only very few computational techniques are reported so far in literture, in addition, a number of tested reactions are very limited. Some computational tools to study these types of reactions are conventional ab initio molecular dynamics (MD) simulations,[63-64] Houk's bond order analysis[65-68], Carpenter's dynamic match analysis[69] and very recently developed Goodman's method.[70-71] The MD technique is quite satisfactory to predict correct bifurcating product selectivities and quantities, but it is very time consuming because relatively a large number of trajectories is necessary for correct quantification. On the other hand, Goodman's method is much less computationally demanding but it requires the optimized structures of all key points from PES (**Scheme 1**), which is sometimes very problematic. The Houk's bond order and Carpenter's dynamic match analyses are so far applied only for a very limited set of reactions and their general applicability is thus largely unknown. In this work, I consider the different set of bifurcating reactions, which includes organic pericyclic reactions, nucleophile substitution *vs*. addition in α-haloketones, Beckmann and Schmidt rearrangements *vs*. fragmentation, and isomeric Pummerer rearrangements and also trifurcating reactions, [20-22,52-56] to predict product ratios from KED using the reactive mode composition factor (RMCF) analysis. Further, I also discuss the limitations of KED and compare its performance with already above-mentioned existing computational protocols.

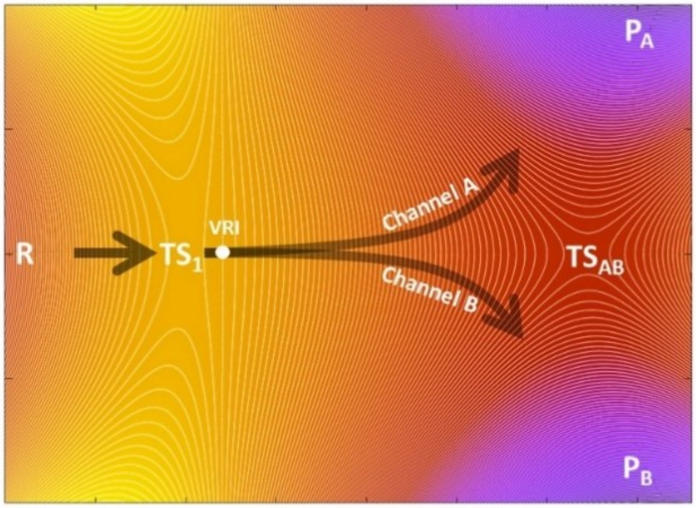

**Scheme 1:** Illustration of the potential energy surface (PES) depicting the distinctive features of a bifurcating reaction. Within the PES, three minima are discernible: one corresponding to the reactant (R), and two associated with the products $P_A$ and $P_B$ and a pivotal transition state ($TS_1$), crucial in determining the reaction rate, is shared by the two competitive product channels, $R \rightarrow P_A$ and $R \rightarrow P_B$. The PES topology is further characterized by the presence of a transition state ($TS_{AB}$) directly connecting $P_A$ with $P_B$, as well as a valley-ridge inflection (VRI).

## 2. Computational methodology:

### 2.1. Density functional theory

Chemistry resides within the vast domain of science that explores the physical and chemical properties of molecules.[72] Although, chemistry has historically been rooted in experimental sciences, however, the emergence of sophisticated software techniques has revolutionized the field, facilitating the resolution of intricate chemical problems through state-of-the-art computational techniques. The discipline of computational chemistry, alternatively sometimes referred as theoretical chemistry involves the investigation of chemical phenomena by using different approximation methods such as Hartree–Fock, post-Hartree–Fock, density functional theory, semiempirical or force field methods to study molecular geometry, chemical reactivity, spectroscopic properties, physical properties of a system etc.[73] The application of computational method in solving chemical problems emerged rapidly, which is reflected in a number of Nobel Prizes in past. In 1998, Walter Kohn was honored Nobel Prize for his pioneering work on density functional theory, and John Pople for his innovative utilization of computational methods in quantum chemistry, exemplified by his development of the Gaussian software package.[74-76] In 2013, Karplus, Levitt, and Warshel were also honored with the Nobel Prize for their significant contributions to the advancement of multiscale models tailored for complex chemical systems.[77-78] The selection of computational approaches relies on several factors, for instances, complexity of molecular systems, the properties under investigation, and the desired level of precision. For small molecules and precise electronic structure description, quantum mechanical-based techniques can be used, while for large systems less computationally intensive methods are necessary. In the former scenario, quantum chemistry approaches from the post-Hartree-Fock (post-HF) realm, such as configuration interaction (CI), complete active space self-consistent field (CASSCF), CASPT2 and coupled cluster (CC) methods, are commonly employed.[79] However, the primary challenge associated with these methods lies in their substantial computational cost and limited applicability to small systems only. On the other hand, for larger systems, density functional theory (DFT) are often used. DFT can be considered as a highly efficient tool for elucidating the electronic structure description of molecules (e.g. molecular geometries, vibrational analysis, spectroscopic studies etc).[80-87] The present work in this thesis for both **Project I** and **II** is mainly based on the use of the DFT methodology and accordingly, a brief introduction of DFT is provided below.

DFT centers around the first Hohenberg-Kohn theorems[82], which elegantly asserts that the precise electronic ground state energy of a system can be deduced entirely from the calculation of its total electron density, denoted as $\rho$(r). This theorem underscores a direct and unequivocal relationship between the electron density of a system and its ground state energy. DFT presents a notable advantage over wave function-based methods in its simplicity and scalability. While wave function approaches necessitate dealing with a function reliant on 4N variables for an N-electron system (three spatial coordinates and one spin coordinate for each electron), DFT reduces this complexity to a mere three variables (x, y, z). This makes DFT notably more suitable for working with larger systems, as the electron density, being the "square of the wave function" ($\rho = \sum_{i=1}^{N} n_i |\psi_i|^2$), can be determined through integration over N–1 electron coordinates, effectively becoming a function of only three variables regardless of the system's electron count. Yet, the challenge within DFT lies in the absence of an exact functional connecting electron density to ground state energy. Variations in electron density can yield different ground state energies, underscoring the need for precise functionals. Consequently, the primary endeavor within DFT-based methodologies is the design and refinement of functionals that accurately bridge electron density with the energy of the ground state.[80-85,88-90]

### 2.1.1. The Hohenberg–Kohn theorems

The essence of the first Hohenberg–Kohn theorem can be stated as "all fundamental properties of a molecule in its lowest electronic state (ground state) are estimated by the ground state electron density function $\rho_0(x, y, z)$". In other words, the ground state energy ($E_0$) can be derived from $\rho_0(x, y, z)$, that is the $E_0$ is a functional of $\rho_0$.[82]

$$\rho_0(x, y, z) \rightarrow E_0 \quad (1)$$

$$E_0 = E[\rho_0] \quad (2)$$

The second Hohenberg-Kohn theorem states that the energy associated with a trial electron density function in DFT is inevitably higher than the exact ground state energy:

$$E_t[\rho_t] \geq E_0[\rho_0] \quad (3)$$

It is necessary to note that $\rho_t$ must satisfy the conditions $\int \rho_t(r)\mathrm{dr} = N$ and $\rho_t(r) \geq 0$ for all $r$ ($r$ is the position vector with coordinates (x, y, z)). In eq 3, the precise functional to calculate ground state energy remains elusive, so DFT methodology use approximate functionals and hence, provides an energy, which is always higher than the actual ground state energy of the system.

## 2.1.2. The Kohn–Sham (KS) theorems

The KS theorem establishes a way to determine ground state electronic properties of the system by calculating its energy and electron density. In the KS approach, an initial estimation of the electron density is considered to calculate the initial guess of the KS orbitals, which are subsequently refined to obtain the final KS orbitals, similar to the Hartree–Fock variational approach. Note that, the ground-state electronic energy of a system is given as the sum of electronic kinetic energies, nucleus–electron interaction energies, and electron–electron repulsion energies, expressed mathematically as follows:

$$E_0 = \langle T[\rho_0] \rangle + \langle V_{Ne}[\rho_0] \rangle + \langle V_{ee}[\rho_0] \rangle \tag{4}$$

In eq 4, the nucleus–electron interaction potential energy term can be demonstrated in terms of a potential known as external potential, $\nu(r_i)$, which relates to the interaction of electron *i* to the nuclei. The nucleus-electron potential energy term is the sum over all *2n* electrons of the potential corresponding to attraction of an electron for all the nuclei (considered as closed-shell molecule with even number of electrons).

$$\langle V_{Ne} \rangle = \sum_{i=1}^{2n} \nu(r_i) \tag{5}$$

Furthermore, the electron density, $\rho$ can also be introduced into $\langle V_{Ne} \rangle$ and hence, $\langle V_{Ne} \rangle$ in eq 5 can be expressed as follows:

$$\langle V_{Ne} \rangle = \int \rho_0(r)\nu(r)\, dr \tag{6}$$

Now, eq 4 can be rearranged by employing the value of $\langle V_{Ne} \rangle$ from eq 6:

$$E_0 = \int \rho_0(r)\nu(r)\, dr + \langle T[\rho_0] \rangle + \langle V_{ee}[\rho_0] \rangle \tag{7}$$

In eq 7, the unknown electronic kinetic energy term, $\langle T[\rho_0] \rangle$ can be expressed by introducing a reference kinetic energy term $\langle T_r[\rho_0] \rangle$, considering the assumption of non-interacting electrons:

$$\Delta\langle T[\rho_0]\rangle = \langle T[\rho_0]\rangle - \langle T_r[\rho_0]\rangle \tag{8}$$

where $\Delta\langle T[\rho_0]\rangle$ represents the difference between the actual kinetic energy and that from the reference system. Also, the 3rd undefined electron-electron repulsion energy term (eq 7), $\langle V_{ee}[\rho_0]\rangle$ can be expressed by considering a known electron–electron repulsion energy from a classical charge–cloud coulomb repulsion energy. This can be expressed mathematically as follows:

$$\Delta\langle V_{ee}[\rho_0]\rangle = \langle V_{ee}[\rho_0]\rangle - \frac{1}{2}\iint \frac{\rho_0(r_1)\rho_0(r_2)}{r_{12}} dr_1\, dr_2 \tag{9}$$

where $\Delta\langle V_{ee}[\rho_0]\rangle$ is the deviation of real electron-electron repulsion energy from reference classical charge–cloud coulomb repulsion energy. Now, substituting eqs 8 and 9 into eq 7, the expression for the energy is:

$$E_0 = \int \rho_0(r)v(r)\, dr + \langle T_r[\rho_0]\rangle + \frac{1}{2}\iint \frac{\rho_0(r_1)\rho_0(r_2)}{r_{12}} dr_1 + \Delta\langle T[\rho_0]\rangle + \Delta\langle V_{ee}[\rho_0]\rangle \tag{10}$$

In eq 10, the differential kinetic energy ($\Delta\langle T[\rho_0]\rangle$) and differential electronic repulsion energy ($\Delta\langle V_{ee}[\rho_0]\rangle$) term can be together represented by a new term $E_{XC}$ known as exchange-correlational energy functional or exchange-correlation energy *i.e.,* $E_{XC}[\rho_0] = \Delta\langle T[\rho_0]\rangle + \Delta\langle V_{ee}[\rho_0]\rangle$. Therefore, eq 10 becomes:

$$E_0 = \int \rho_0(r)v(r)\, dr + \langle T_r[\rho_0]\rangle + \frac{1}{2}\iint \frac{\rho_0(r_1)\rho_0(r_2)}{r_{12}} dr_1\, dr_2 + E_{XC}[\rho_0] \tag{11}$$

A detailed description of each term in eq 11 can be explained as follows:

(*i*) The first term, which involves integrating the product of the electron density and the external potential, can alternatively be expressed as:

$$\int \rho_0(r)v(r)\, dr = -\sum_{Nuclei\ A} Z_A \int \frac{\rho_0(r_1)}{r_{1A}} dr_1 \tag{12}$$

(*ii*) The second term represents the reference kinetic energy for non-interacting electrons, which can be formulated in terms of spatial Kohn-Sham (KS) orbitals $\Psi_i^{KS}$ through the application of Dirac and Slater-Condon principles:

$$\langle T_r[\rho_0]\rangle = -\frac{1}{2}\sum_{i=1}^{2n} \langle \Psi_i^{KS}(1) \left| \nabla_1^2 \right| \Psi_i^{KS}(1)\rangle \tag{13}$$

(*iii*) The third term corresponds to the classical electrostatic repulsion.

(*iv*) The fourth term is the exchange-correlation energy functional, $E_{XC}[\rho_0]$ and holds the key: if this were known, DFT would furnish the precise total energy, encompassing electron correlation effects. However, the challenge lies in crafting a precise $E_{XC}[\rho_0]$ functional from an energy density that remains unknown, thus constituting the primary hurdle in the DFT methodology.

Finally, eq 11 can be expressed in more detail as follows:

$$E_0 = -\sum_{Nuclei\ A} Z_A \int \frac{\rho_0(r_1)}{r_{1A}} dr_1 \langle T_r[\rho_0]\rangle - \frac{1}{2}\sum_{i=1}^{2n} \langle \Psi_i^{KS}(1) \left| \nabla_1^2 \right| \Psi_i^{KS}(1)\rangle + \frac{1}{2}\iint \frac{\rho_0(r_1)\rho_0(r_2)}{r_{12}} dr_1\, dr_2 + E_{XC}[\rho_0] \tag{14}$$

Thus, to solve the problem regarding the unknown exchange-correlation energy functional, $E_{XC}[\rho_0]$, an important approximation is used in DFT. This was presented by Kohn and Sham and known now as Kohn-Sham equations. The KS equations are derived from the variation theorem, ensuring that the electron density in the reference system matches that of the real non-interacting one electron system. This can be expressed as one-electron orbitals or KS orbitals, eq 15. The main idea of the Kohn-Sham approximation is to derive a fictitious local effective external potential that allows for calculating the ground-state density and energy of interacting electron systems.

$$\rho_0 = \rho_r = \sum_{i=1}^{2n} |\Psi_i^{KS}(1)|^2 \tag{15}$$

Combining eqs 14 and 15 yields the derivation of the KS equations:

$$\left[-\frac{1}{2}\nabla_i^2 - \sum_{nuclei\ A} \frac{Z_A}{r_{1A}} + \int \frac{\rho(r_2)}{r_{12}} dr_2 + v_{XC}(1)\right] \Psi_i^{KS}(1) = \epsilon_i^{KS} + \Psi_i^{KS}(1) \tag{16}$$

Here, $\epsilon_i^{KS}$ and $v_{XC}$ represent the KS energy levels and the exchange-correlation potential, respectively. The exchange-correlation potential, $v_{XC}$, can be defined as the functional derivative of the exchange-correlation energy, $E_{XC}[\rho(r)]$, with respect to the electron density, $[\rho(r)]$.

$$v_{XC}(r) = \frac{\delta E_{XC}[\rho(r)]}{\delta \rho(r)} \tag{17}$$

In eq 17, the term $E_{XC}[\rho(r)]$ can be decomposed into two distinct components: pure exchange, denoted as $E_X$, and correlation part, denoted as $E_C$. Nonetheless, a fundamental challenge in DFT arises from the lack of understanding regarding the exact exchange-correlation energy functional. Consequently, DFT resorts to approximations within the Hamiltonian operator to formulate a diverse range of exchange-correlation energy functionals.

The choice of functional in DFT depends on the specific system being studied and the properties of interest. The simplest approximation is used to calculate exchange-correlation energy functional, $E_{XC}[\rho(r)]$ in DFT is the local density approximation (LDA).[91] In LDA the electron density is considered as an uniform electron gas or slowly varing function with respect to the position. Within LDA, both the term $E_{XC}[\rho(r)]$ and its derivative, $\upsilon_{XC}^{LDA}$, can be precisely determined. Another improved version of the LDA functional is the generalized gradient approximation (GGA). In real-system scenarios, the electron density within the atoms or molecules varies across the space, deviating from the uniform electron gas. GGA improves LDA by considering not only the local electron density but also its gradient (first derivatives with respect to the position). This allows for better treatment of bonding and structural properties. The examples of gradient-corrected functionals are B88[92], G96[93-94], LYP[95], P86[96], PW86[97], PW91[98] etc. Another development after GGA is the meta-GGA functionals. Meta-GGA functional includes the second derivative of the electron density, whereas GGA considers only the first derivative in the exchange–correlation potential.[99] Further, improvements in DFT is the development of hybrid functionals, where a fraction of exact exchange energy of the exchange-correlational energy functionals is calculated from Hartree–Fock theory. This “hybridization” mainly enhances the accuracy of DFT calculations by incorporating some of the non-local exchange effects that are not fully captured by pure DFT functionals like LDA or GGA. Throughout this thesis for both **Project I** and **II**, I employed the advantage of the three-parameter B3LYP hybrid functional[100] as they often provide more accurate results for a wide range of properties. The B3LYP functional combines the Becke three-parameter exchange functional (B3) with the Lee-Yang-Parr correlation functional (LYP).[100]

### 2.1.3. Basis set

A basis set comprises a collection of mathematical functions, known as basis functions, employed to construct atomic orbitals. The linear combination of these atomic basis functions gives rise to molecular orbitals or electron distributions within a molecule, commonly referred to as the linear combination of atomic orbital (LCAO) approach. Generally, the performance of a basis set is better as its size increases (larger basis sets). Therefore, selecting an appropriate basis set is crucial for achieving accurate results with a given functional. In electronic structure analysis, two types of basis functions are typically utilized: Slater Type Orbitals (STO)[101] and Gaussian Type Orbitals (GTO)[102]. Gaussian type functions differ from Slater functions primarily in the exponential part, with the former involving the square of the radius ($r^2$). When comparing STO with GTO, STO exhibits superiority in two key aspects. Firstly, STO includes a cusp at the nucleus, contrasting with the absence of a zero slope at the nucleus in GTO. Secondly, GTO exhibits a rapid decay far from the nucleus compared to STO. Moreover, utilizing a single GTO often results in an inadequate representation of the basis set, leading to less accurate outcomes. Conversely, employing pure STO can be excessively time-consuming due to the considerable computational resources required to handle complex integral functions. To address this challenge, a solution involves using a linear combination of GTOs with various exponents and coefficients as basis functions to approximate a particular Slater type function. Such basis sets are commonly referred to as STO–nG type basis sets, with 'n' representing the number of Gaussian primitives employed to fit a specific STO.

Basis sets can be categorized into two main types: minimal and extended basis sets. Minimal basis sets are the simplest, employing the same number of Gaussian primitives for both core and valence orbitals within a single basis function. An example of a minimal basis set is STO–3G.[103] Conversely, extended basis sets offer a more detailed analysis of each atomic orbital by comprising more than one basis function, each characterized by its unique coefficient. For instance, the double-zeta (DZ) basis set includes two basis functions per atomic orbital, making it twice as large as the minimal basis set. Extended basis sets encompass various types, such as split-valence, polarized, diffuse, and correlation consistent sets. Each type serves specific purposes in achieving accurate results in electronic structure calculations. Below is a brief overview of different types of extended basis sets.

Within extended basis sets, the concept of doubling all basis functions is encapsulated in the *Double Zeta* (DZ) basis set, with "zeta" derived from the exponent of orbital basis functions ($\zeta$). For instance, in a DZ basis set, there are two s-functions for hydrogen (1s and 1s') and four for helium (1s, 1s', 2s, and 2s'). The next advancement is the *Triple Zeta* (TZ) basis, which includes three basis functions to define an orbital. For example, the TZ basis for first-row elements consists of six s-functions and three p-functions. Beyond the TZ basis, further extensions include *Quadruple Zeta* (QZ) and *Quintuple Zeta* (5Z), etc.

The *split valence* basis set is a variant of extended basis sets that segregates valence and core orbitals, treating them with distinct sets of basis functions. For instance, in the 3-21G *split valence* basis set[104], the basis functions for inner and outer shells are represented by two and one Gaussian primitives, respectively. Additionally, each core orbital is represented by a single basis function, composed of three Gaussians. Examples of split valence basis sets include 6-31G[105] and 6-311G[106-107], which represent *double* and *triple zeta split valence* basis sets, respectively, and further enhance the accuracy of electronic structure calculations.

For molecules containing heavier atoms, the presence of neighboring atoms distorts the electronic environment, disrupting the spherical symmetry of atomic orbitals. This distortion arises from the charge distribution in the molecule, leading to a polarization effect. To accommodate such scenarios, basis sets incorporate additional functions known as *polarization functions*, denoted by an asterisk (*). The inclusion of *polarization functions* enhances the flexibility of the basis set, allowing molecular orbitals to exhibit greater asymmetry around the nucleus. For instance, in the 6-31G* basis set, the asterisk signifies the introduction of p-orbitals to heavier atoms to reflect polarization. In some cases, it becomes necessary to introduce polarization functions even for lighter atoms like hydrogen and helium, denoted by double asterisks (**).[108-109] Similarly, d-orbitals introduce polarization for p-orbitals, while f-orbitals influence the polarization of d-orbitals, and so forth. This approach ensures that basis sets adequately capture the molecular environment's complexity, especially in systems involving heavier atoms.

In systems featuring heteroatoms, anions, lone pairs, or weak bonds like hydrogen bonds, electrons involved in bonding are often loosely bound to the nucleus. To accurately represent such systems, a specialized basis set known as *diffuse functions* is employed, denoted by a plus sign '+'. *Diffuse functions* are characterized by very small exponent values, resulting in slow decay with distance from the nucleus. This property enables them to describe bonding more accurately in situations where electron density extends further from the nucleus. Typically, *diffuse functions* include s and p types. In notation such as 3-21+G* or 6-31+G*, the addition of one plus sign indicates the inclusion of one diffuse s-type and p-type gaussian with the same exponents on heavy atoms. Conversely, the presence of two plus signs '+ +' signifies the addition of one diffuse s-type and p-type gaussian on heavy atoms and one diffuse s-type Gaussian function on hydrogen or helium. This approach ensures an effective representation of systems with dispersed electron density.

Computing systems involving heavier atoms, typically third-row elements or beyond in the periodic table, presents greater complexity compared to lighter ones. This complexity arises from the increased number of two-electron integrals and the impact of relativistic effects. As a result, employing all-electron basis sets for such systems becomes highly intricate and time-consuming. To overcome these challenges, the *Effective Core Potential* (ECP), also known as *Pseudopotential*, approach is utilized. In ECP, core electrons are approximated using a suitable function, often an average potential that incorporates relativistic effects.[110] This approximation enables the explicit treatment of valence electrons without sacrificing the result accuracy. In ECP-incorporated basis functions, pseudo-orbitals accurately represent the outer part of the atom while lacking a nodal structure in the core region. When dealing with systems containing heavier elements, employing ECP not only incorporates relativistic effects but also substantially reduces computational expenses by accurately approximating the core electrons, which are often less critical for investigating many chemical properties. Examples of basis sets that incorporate ECP include LANL2DZ,[111-113] SDD,[114-116] and others. These sets are designed to efficiently handle the complexities associated with heavier elements, ensuring accurate results while minimizing computational resources.

## 2.2. Specifics of DFT calculations used in the thesis

In the two presented projects, I applied DFT to study molecular properties, reaction energetics, reduction potentials, KED and wherever possible I compared their results with available experimental data. I carried out geometry optimizations and frequency calculations of all the structural models in the presence of the implicit conductor-like polarizable continuum model (CPCM)[117] to mimic the solvent environment (if present). More explicitly, all the structures were optimized using hybrid B3LYP[100] functional. Regarding the basis set, I used all electron Karlsruhe valence triple-zeta polarization, def2-TZVP basis set for the range of bifurcating reactions considered in this study (**Project II**).[118-119] On the other hand, I considered general basis sets for native F430 and four bio-synthetic intermediate precursors (**Project I**). Namely, for Ni atom, I used effective core potential (ECP) included LANL2TZ[111-113] (Los Alamos National Laboratory 2 double ζ) basis set while all electron Pople's basis sets for all other non-metal systems.[120] In this study, I used 6-311G* for key atoms involved in reactivity (the $SCH_3$ and SH groups of the $H_3CS$–

CoM and truncated CoB-SH substrates, respectively), and 6-31G* for the rest.[120] Specifically, to obtain better description of electronic energies, I used a larger basis set. I performed single-point calculations on top of the optimized geometries, consequently using LANL2TZ+ ECP for metal atom and 6-311++G** for the rest.[111-113,120] This general modeling methodology employed here has been carefully examined and successfully applied, on the basis of a literature review and was found to be suitable for large number of metalloenzymes.[44-45,121] Further, dispersion effects were evaluated with D3 version of Grimme's dispersion correction coupled with the original D3 damping function.[122] On top of each optimized geometry, I performed frequency calculation (*i*) to characterize the nature of a structure, (*ii*) to evaluate thermal contributions to the Gibbs free energy of a system and (*iii*) to evaluate KED as in detail introduced later in the thesis (Section 4.2.). The relevant transition states were ensured to have only one imaginary frequency, which was further confirmed by performing intrinsic reaction coordinate analysis. The reaction free energies were evaluated from optimized geometries using eq 18.

$$G = E_{el,solv} + [E_{ZPVE} + pV - RTlnQ] \tag{18}$$

where $E_{el,solv}$ is the calculated potential energies in solution, the $[E_{ZPVE} + pV - RTlnQ]$ term corresponds to the thermal enthalpic and entropic contributions of the solute energy with $E_{ZPVE}$ and $Q$ corresponding to zero-point vibrational energy correction and the molecular partition function (*i.e.* product of the vibrational, rotational, and translational partition functions), respectively. In the upcoming section for both projects, I considered eq 18 to calculate reduction potentials and reaction energetics.

Atomic charges and delocalization indices were determined by integration of the DFT-optimized electron density, utilizing the atoms-in-molecules (AIM) methodology as implemented in the AIMAll program.[123] Atomic basins were integrated employing the Proaim method,[123] utilizing a "Fine" interatomic surface mesh, an outer angular integration quadrature of 7200 grid points, and a maximum integration radius of 13.0 Bohr were considered for all atoms.

## 2.3. Calculation of reduction potential

The reduction potential is a crucial electrochemical quantity, especially in the context of redox reactions. It provides valuable information about the driving forces for electron transfers between reacting entities. This quantity is also one of the main reactivity factors studied in **Project I** (section 5.1.).

The one-electron reduction potential is a measure of the ability of a chemical species to readily receive a single electron. It can be calculated by the difference in Gibbs free energies between the oxidized and reduced form of species:

$$E^{O}[V] = \frac{G_{ox}[eV] - G_{red}[eV] - FE^{O}_{abs}(reference)[eV]}{F} \tag{19}$$

where ox/red denotes oxidized/reduced state of the solute. $F$ is referred to as Faraday constant and $E^{O}_{abs}$ stands for considered absolute reference potential. Note that the Gibbs free energy values for oxidized and reduced species, $G_{ox}$ and $G_{red}$ from eq 19, are calculated according to eq 18. As for the absolute reference potential in eq 19, I used normal hydrogen electrode (NHE) in water with the value of $E^{O}_{NHE} = 4.28\ eV$.[124]

## 3. Construction of structural models:

**Project I** deals with enzymatic reactions but a complete quantum mechanical treatment of the entire enzyme is completely out of current possibilities. Therefore, prior to conducting any calculations, it is mandatory to construct a reliable structural model to represent properly the enzymatic active site.[125] One such approach that considered extensively in bioinorganic systems is combined quantum mechanics/molecular mechanics (QM/MM) approach.[126-132] Another extensively used methods in scientific community for treating such systems is the so-called ‘cluster model’ approach.[44,121,133-135] The benefit for considering cluster model in studying reactivity/energetics is that it allows for the identification of all relevant structural changes and minima as well as proper representation of reaction region using simple dielectric continuum with a small dielectric constant (e.g. $\varepsilon \sim 4 - 10$).

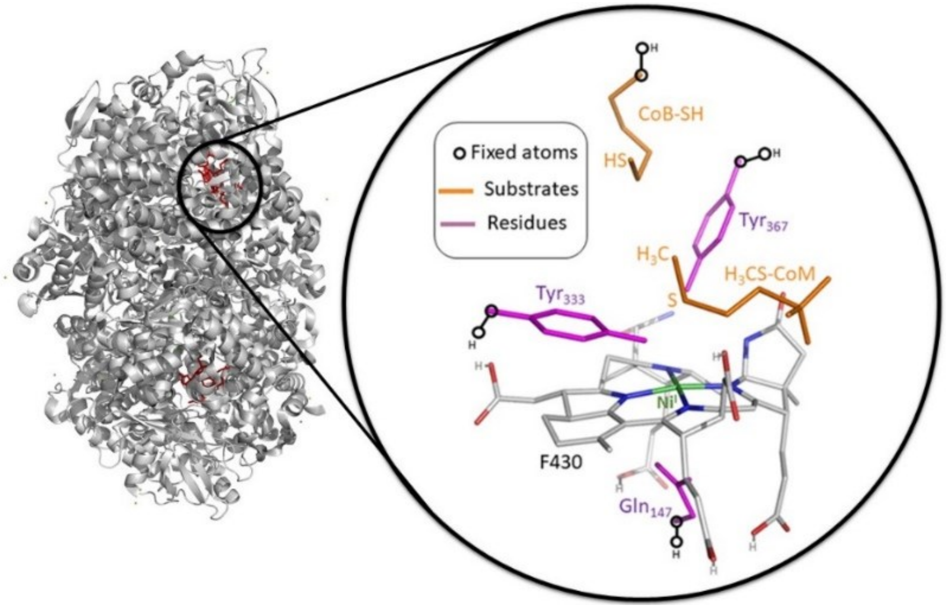

**Figure 4:** A cluster model of the MCR active site has been carefully constructed based on a high-resolution crystal structure (PDB code 1HBN). Hydrogen atoms are not displayed in the figure to enhance clarity and resolution. Amino acid residues under consideration (Tyr333, Tyr367, and Gln147) and the substrate CoB–SH have been truncated and capped with hydrogen atoms. This cluster model, which includes the native F430 cofactor, is referred to in this study as model **E**, a nomenclature adopted for the sake of simplification.

A model of the native MCR active site (denoted as **E**) was constructed from the available crystal X-ray data-based structure with PDB code 1HBN. Our cluster model contains total 190 atoms consisting of (*i*) the whole Ni-containing F430 cofactor (*ii*) methyl and hydrogen donor substrates $CH_3$–SCoM and CoB–SH, respectively and (*iii*) the essential neighboring amino acid residues (Tyr333, Tyr367 and Gln147), as shown in **Figure 4**. I applied some truncations to reduce the size of the model for computational feasibility. I kept the F430-cofactor, substrate $CH_3$–SCoM as a whole, while Gln147 and Tyr residues were represented by propionamide and *p*-cresols (4-methylphenols), respectively. Carboxylic groups of the F430 cofactor were kept protonated during all calculations, if not stated otherwise. The calculated total charge of the MCR model as -1. In analogy with the native model **E**, I built the cluster models anchoring the four non-native coenzymes **A**–**D** (labels introduced earlier in **Figure 2**), by modifying the native F430 active site (**E**, in **Figure 4**).

# 4. Theory in chemical reactivity:

## 4.1. Statistical transition state theory (TST)

TST is the cornerstone in the field of chemical kinetics, which provides a framework for understanding the rates of chemical reactions. It provides a conceptual idea that connects the microscopic realm of atoms and molecules with the macroscopic observations of reaction rates and kinetics. TST was developed in the 1930s[4,136-137] that deals with the understanding of reaction rate for elementary chemical reaction by dividing the reaction region into two distinct space called the reactant region (RR) and product region (PR).[138] The reactant region is confined to the initial region where the system can be found before reacting while the product region defines the final region that achieved after accomplishment of the reaction. The interface between the two regions is commonly known as the transition state. This fleeting state represents the highest energy point along the reaction coordinate, where bonds are in the process of breaking and forming.[138] TST also reveals the relationship between thermodynamics and kinetics—a vital aspect in comprehending chemical processes.[6] The fundamental aspects of TST can be stated as follows:

(i) Separation of electronic and nuclear movement (similar to the Born-Oppenheimer approximation).

(ii) Rate of the reaction can be investigated by examining the formation of activation complex near the saddle point in the potential energy surface (PES). The saddle point is usually referred as the transition state.

(iii) The activated complex must be in equilibrium with the reactant system.

(iv) Once reactants complex is converted to the transition state, it does not collapse back to the structure of reactants. In other words, TST ignores recrossing events completely.

(v) TST assumes the formation of long-lived intermediates along the reaction coordinate. It considers the Boltzmann distribution of energies for reactants and transition states.

The route of development of TST can be enlightened from the derivation of empirical Arrhenius equation.[139-141] Arrhenius equation provided a groundbreaking relationship between the temperature and the rate constant of a reaction. It postulated that the rate constant of a reaction exponentially increases either with increase in temperature, or decrease in activation energy. In other words, Arrhenius equation is a notion for the temperature dependence of reaction rates (as shown in eq 21).

$$\frac{d\,lnk}{dT} = \frac{\Delta E}{RT^2} \tag{20}$$

Integration of eq 20 leads to the Arrhenius equation (eq 21).

$$k = Ae^{\frac{-E_a}{RT}} \tag{21}$$

here, $k$ is the rate constant, $T$ is the absolute temperature, $A$ is the pre-exponential factor or Arrhenius factor (sometimes also referred as frequency factor) and $E_a$ is the molar activation energy of the reaction. Prior to the advent of TST, the Arrhenius rate law was extensively employed to ascertain the energies associated with the reaction barrier. However, the Arrhenius equation was limited in its scope, as it did not account for the effects of changes in entropy during the transition state of a reaction. Also, the Arrhenius equation is rooted in empirical observations and overlooks mechanistic complexities, such as the potential involvement of reactive intermediates in the transformation from reactant to product.[142] Hence, to elucidate the two key parameters associated with this law: the pre-exponential factor ($A$) and the activation energy ($E_a$), leads to the development of TST. TST, which culminated in the development of the Eyring equation (eq 22), effectively tackles these challenges. The Eyring equation introduces the notion of the free energy of activation, which combines both enthalpic and entropic contributions:

$$\begin{aligned} k &= \frac{k_b T}{h} e^{-\frac{\Delta G^\ddagger}{RT}} \\ &= \frac{k_b T}{h} e^{\frac{\Delta S^\ddagger}{R}} e^{-\frac{\Delta H^\ddagger}{RT}} \end{aligned} \tag{22}$$

the term $h$ and $k_b$ represent Planck and Boltzmann constants respectively, $\Delta G^{\neq}$is the Gibbs free energy of activation ($\Delta G^{\neq}$ can be estimated from eq 18) and $\Delta H^\ddagger$ and $\Delta S^\ddagger$ represent the enthalpy and entropy of activation respectively. Alternatively, the Eyring equation can also rewritten:

$$ln\,\frac{k}{T} = \frac{-\Delta H^\ddagger}{R} \cdot \frac{1}{T} + ln\frac{k_b}{h} + \frac{\Delta S^\ddagger}{R} \tag{23}$$

eq 23 can be considered to evaluate the reaction rate at different temperatures. The graphical plot of $ln\left(\frac{k}{T}\right)$ $vs$ $\frac{1}{T}$ provides a straight line with slope and intercept $\frac{-\Delta H^\ddagger}{R}$ and $ln\frac{k_b}{h} + \frac{\Delta S^\ddagger}{R}$ respectively from which enthalpy and entropy of activation can be determined.

## 4.2. Reactive mode composition factor (RMCF) analysis

RMCF analysis provides insight into the kinetic energy distribution (KED) within a reactive mode, generally within any normal mode featured by a real or imaginary frequency. In order to understand the applicability of the RMCF analysis to non-TST reactions studied in **Project II**, I will first give here its physical background (the theory also provided in Ref 143).

Using the harmonic approximation within a normal-mode vibrational analysis (frequency calculation), vibrational coordinates $Q_\alpha$ can be expressed in term of mass-weighted atomic displacement $\vec{r_j}\sqrt{m_j}$ of the $j^{\text{th}}$ atom.

$$Q_\alpha = \sum_{j=1}^{n} \vec{e}_{j\alpha}\, \vec{r_j}\, \sqrt{m_j} \tag{24}$$

$\vec{e}_{j\alpha}$ denotes a set of orthogonal unitary vectors, which represents the motion of $j^{\text{th}}$ atom in the $\alpha$ mode. Alternatively, $\vec{e}_{j\alpha}$ can be expressed in terms of atomic kinetic energy of the $j^{\text{th}}$ atom $\langle T_j \rangle$, related to the linear combination of kinetic energy of all kinds of modes $\langle T_\alpha \rangle$,

$$\langle T_j \rangle = \sum_\alpha e_{j\alpha}^2 \langle T_\alpha \rangle = \sum_\alpha \mathrm{KED}_{j\alpha} \langle T_\alpha \rangle \tag{25}$$

Eq 25 clearly demonstrates how kinetic energy of the $j$-th atom is dispersed over the normal modes of the molecular system. Further, $e_{j\alpha}^2$ can be represented as the fraction of kinetic energy of the mode $\alpha$ for the displacement of atom $j$. I described it as atomic kinetic energy distribution factor ($\mathrm{KED}_{j\alpha}$) associated with the $j$-th atom in the mode α with real or imaginary frequencies and thus, it is easily accessible to the transition states as well. KED values can be derived from the cartesian atomic displacements $\vec{r_j}$ associated with the mode $\alpha$.

$$\mathrm{KED}_{j\alpha} = \left( \frac{m_j r_j^2}{\sum_k^n m_k r_k^2} \right)_\alpha \tag{26}$$

where $m_j$ and $r_j$ are the mass and cartesian displacement of the $j^{\text{th}}$ atom respectively.

This method is straightforward to use, as it only requires the optimization of one transition state, TS, and its vibrational analysis. Within the reactive mode ($\alpha$ = RM), the sum of over all the KED factors (KED values associated with atoms) is normalized so, equal to one, $\sum_{k=1}^{n} \mathrm{KED}_{\mathrm{k,RM}} = 1$ (n is total number of atoms in the system).

In the section focused on Essential results of **Project II** (section 6), I will more explicitly explain the application of KED to predict the product selectivity of bifurcations reactions, as well as I will discuss its limitation and advantage compared to other computational techniques.

# 5. Essential results of Project I:

## 5.1. Redox potentials: Models with the native F430 (E) *vs.* biosynthetic precursors of F430 (A–D)

For the Ni center in F430 to be catalytically competent, it must be in the +I oxidation state, but during the catalytic cycle it changes its oxidation state between +I and +II. This actually motivated me to investigate the redox property of F430 and its presumably important role in catalysis. To this aim, I calculated *E*° for native F430 (**E**) and its biosynthetic precursors (**A**–**D**) to understand how nature compel F430 as unique catalyst for methane production compared to all four biosynthetic precursors (**Figure 2**). Notably, such a hypothesis is only tenable if the chemical alterations introduced to the porphyrin framework during the biosynthetic pathway of F430 lead to noteworthy shifts in its standard reduction potential. I proceeded the computational methodology from (eq 19) to evaluate *E*° for native F430 (**E**) and its biosynthetic precursors (**A**–**D**). All the results are listed in **Table 1**. The table contains *E*° for the enzymatic cluster models (**A**–**E**) as well as spin-state energetics of these sites in their oxidized/reduced forms.

It is evident from **Table 1** that there is a remarkable change in *E*° across whole series from **A**–**E**. A close inspection reveals that the early-stage bio-synthetic complexes (**A** and **B**) exhibit significant reducing strength, whereas the native active site containing F430 (**E**) stands out as the strongest oxidizing agent within the series. I obtained the variation of *E*° across the series that is approximately ~ 1.5V. As for the spin energetics of the oxidized and reduced forms of models **A**–**D**, the triplet and doublet spin states are more stable compared to the singlet and quartet ones, respectively. In case of the reduced form of **E**, I also calculated the doublet state to be significantly more stable than the quartet one (20 kcal mol$^{-1}$), while energies of the singlet and triplet state of the oxidized form of **E** are almost the same (~1 kcal mol$^{-1}$, in **Table 1**), with singlet to be the ground state. Consistent with the trend observed for the reduction potential in the **A**–**E** series, the energy gap between the Ni$^{II}$ singlet and triplet evolves similarly. This implies that the stability of the triplet state of Ni$^{II}$ decreases in the order **B** > **A** > **C** > **D** > **E**.

Finally, it is important to summarize that the biosynthetic changes on the macrocyclic ring of the Ni complex (from **A** to **E**) yield a substantial influence on Ni atom redox property. This prompted me to delve into its impact on reactivity in MCR catalytic cycle (from **A**–**E**) in the subsequent sections.

**Table 1**: Redox potentials, $E°$ (from eq 19) for the couple $Ni^{II}/Ni^{I}$ in all cluster models **A**–**E** from **Figure 2**. $E°$ are calculated with respect to normal hydrogen electrode (NHE), as a reference .[124] It also contains the ground spin state and the spin-state energetics for the oxidized and reduced forms of Ni-containing complexes.

| Cluster model | $S_{ox}/S_{red}$ | $E°_{calc}$ (V) | Oxidized form: Singlet/triplet gap (kcal mol$^{-1}$) | Reduced form: Doublet/quartet gap (kcal mol$^{-1}$) |
|---|---|---|---|---|
| **A** | 1 / ½ | -1.77 | 5.8 | 12.8 |
| **B** | 1 / ½ | -1.95 | 6.7 | 12.9 |
| **C** | 1 / ½ | -1.11 | 4.9 | 17.2 |
| **D** | 1 / ½ | -0.88 | 1.8 | 26.9 |
| **E** | 0 / ½ | -0.53 | 0.9 | 20.0 |

## 5.2. Evaluation of reaction energetics of the uncatalyzed reaction

From the very beginning of the project, we were interested in understanding the competence of the F430 *vs.* F430 biosynthetic precursors for methane production. Therefore, as a reference case, I first studied the uncatalyzed in-water reaction between $CH_3S$–CoM and CoB–SH substrates in the absence of Ni-macrocycle. **Figure 5** clearly illustrates that this particular reaction can never occur without the involvement of the Ni-porphyrin system, as evidenced by the very high free energy barrier associated with it, ($\Delta G^{\neq}$ ~89 kcal mol$^{-1}$). The calculated free energy of the reaction is exergonic ($\Delta G_0 = -4.6$ kcal mol$^{-1}$). The overall process can be explained as a single step process with one barrier (**Figure 5**), where a transition state features the simultaneous formation of $CH_4$ and the heterodisulfidic product.

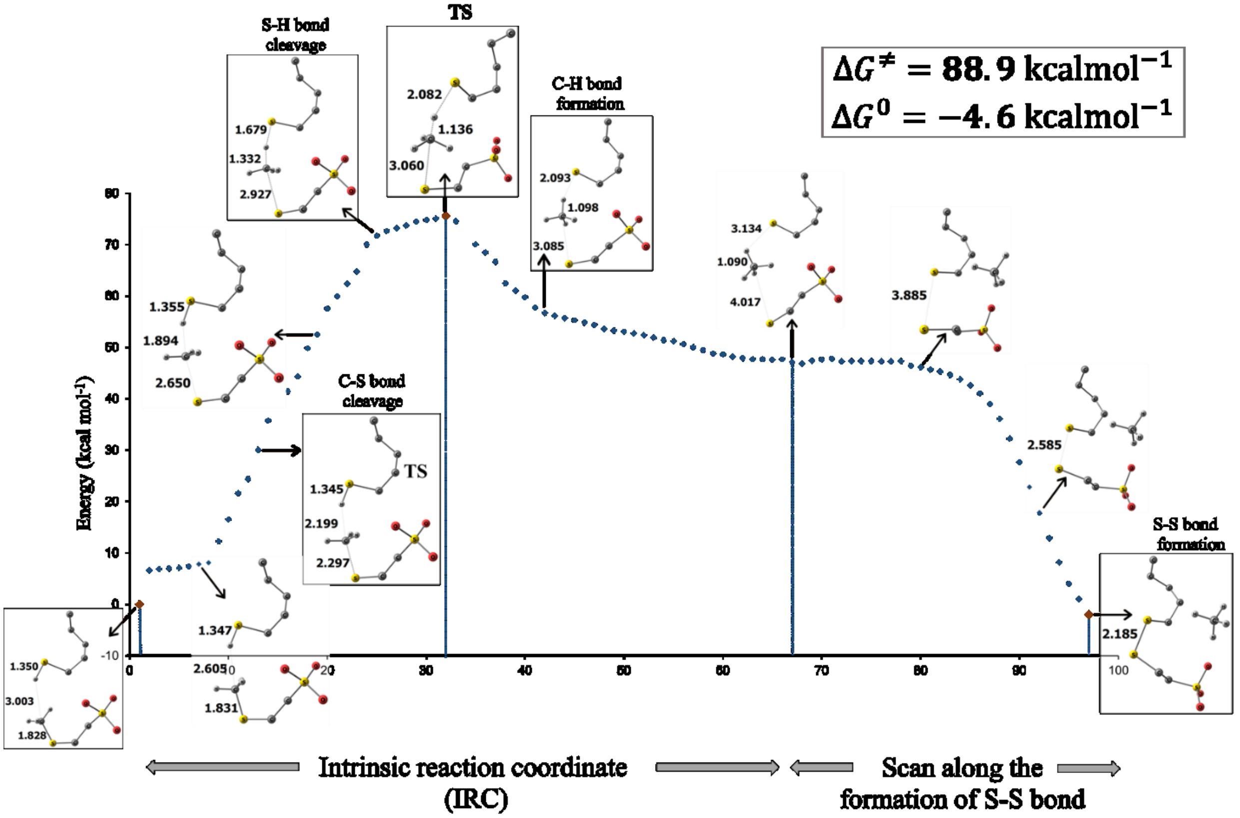

**Figure 5:** Potential energy surface for uncatalyzed reaction between the $CH_3S$–CoM and CoB–SH (*i.e.*, in the absence of Ni-macrocycle). The intrinsic reaction coordinate (IRC) encompasses three key events (single-barrier): the S−$CH_3$ and S−H bond cleavage and $CH_4$ formation. For the next step, involving the S−S bond formation, I performed scan calculations which suggest that this step is nearly barrier free. Key structures with some selected interatomic distances (in Å) along the reaction coordinate are shown. The structures within the box illustrate the initial stages of achieving the cleavage and formation of S−$CH_3$, S–H, C–H and S–S bond respectively. The overall free energy (in kcal mol$^{-1}$) of the reaction ($\Delta G_0$) and barrier ($\Delta G^{\neq}$) are also provided in **Figure 5**.

## 5.3. Evaluation of reaction energetics in models with the native F430 cofactor *vs.* biosynthetic precursors of F430

To investigate the energetics of the reaction in active-site models **A**–**E** (*i.e.*, in the presence of the Ni-porphyrin complexes), I took advantage of the consensual mechanism as illustrated in **Figure 3** to unravel the enigma behind the involvement of catalyst for catalytic $CH_4$ formation. I evaluated the reaction energetics and identified all the minima and transition states along the reaction coordinate for native F430-anchoring enzymatic model (**E**) and its four bio-synthetic precursors (**A**–**D**). The overall catalytic mechanism consists of three consecutive steps, each associated with the individual barrier. The first catalytic step is very crucial for methanogenesis and it determines the full-reaction rate. From **Figure 6**, this step initiates with the formation of a transient methyl radical through the dissociation of the $CH_3$–S bond in coenzyme M, with a direct involvement of the Ni center. The mechanism of **step 1** can be divided into three following events that occur concertedly: (*i*) Ni atom alters its oxidation state from I to II (*ii*) the $CH_3$–S bond is cleaved and (*iii*) the $Ni^{II}$–S bond is formed. The observed chemical events strongly imply that modifications to the macrocyclic ring are likely to exert a notable impact on the barrier of this step ($\Delta G_1^{\neq}$). It is evident from **Figure 6** that the variation of $\Delta G_1^{\neq}$ across the series **A** to **E** is quite significant where I obtained the lowest $\Delta G_1^{\neq}$ for native F430-containing model **E** (~20 kcal mol$^{-1}$) and the highest one for **B** (almost twice, ~38 kcal mol$^{-1}$). Notably, the calculated value of $\Delta G_1^{\neq}$ decreases monotonously as moving from early stage precursors to final maturation of the cofactor, following the evolution **B** > **A** > **C** > **D** > **E**. This result implies that each step of F430 biosynthesis is very important and evolutionarily optimized, so that eventually, the whole biosynthesis ends at the final F430 structure, allowing efficient $CH_4$ formation. Similar to $\Delta G_1^{\neq}$, I observed across the series **A**–**E** the same variation of free energy of reaction ($\Delta G_{0,1}$) for **step 1**, leading to the intermediate $Int_1$ with the transient methyl radical. In fact, there is a one-to-one correlation obtained between $\Delta G_1^{\neq}$ and $\Delta G_{0,1}$ (~1:1) for the **step 1**, which correlates with the geometric- and electronic-structure resemblance between the transition state $TS_1$ and the intermediate $Int_1$ (*i.e.*, along the reaction coordinate $TS_1$ is late and close to intermediate methyl species). It is important to point out that in **step 1** the oxidized Ni center in all models is in the triplet spin state ($S_{Ni^{II}} = 1$), engaging in antiferromagnetic coupling with the transient $CH_3$ radical.

In addition to analysis of energetics for **step 1**, I conducted RMCF analysis of the kinetic energy distribution within the reactive mode of the $TS_1$ and correlated with the other molecular properties (as discussed later). An interesting finding reveals that the transient methyl radical generated during the reductive cleavage of S−$CH_3$ bond accumulates kinetic energy of the reactive mode, with the highest KED ($KED_{CH_3}$) for native cofactor associated model **E** (0.880), while for **B** is the lowest (0.788). This outcome corroborates that the shallow $Int_1$ state can be circumvented

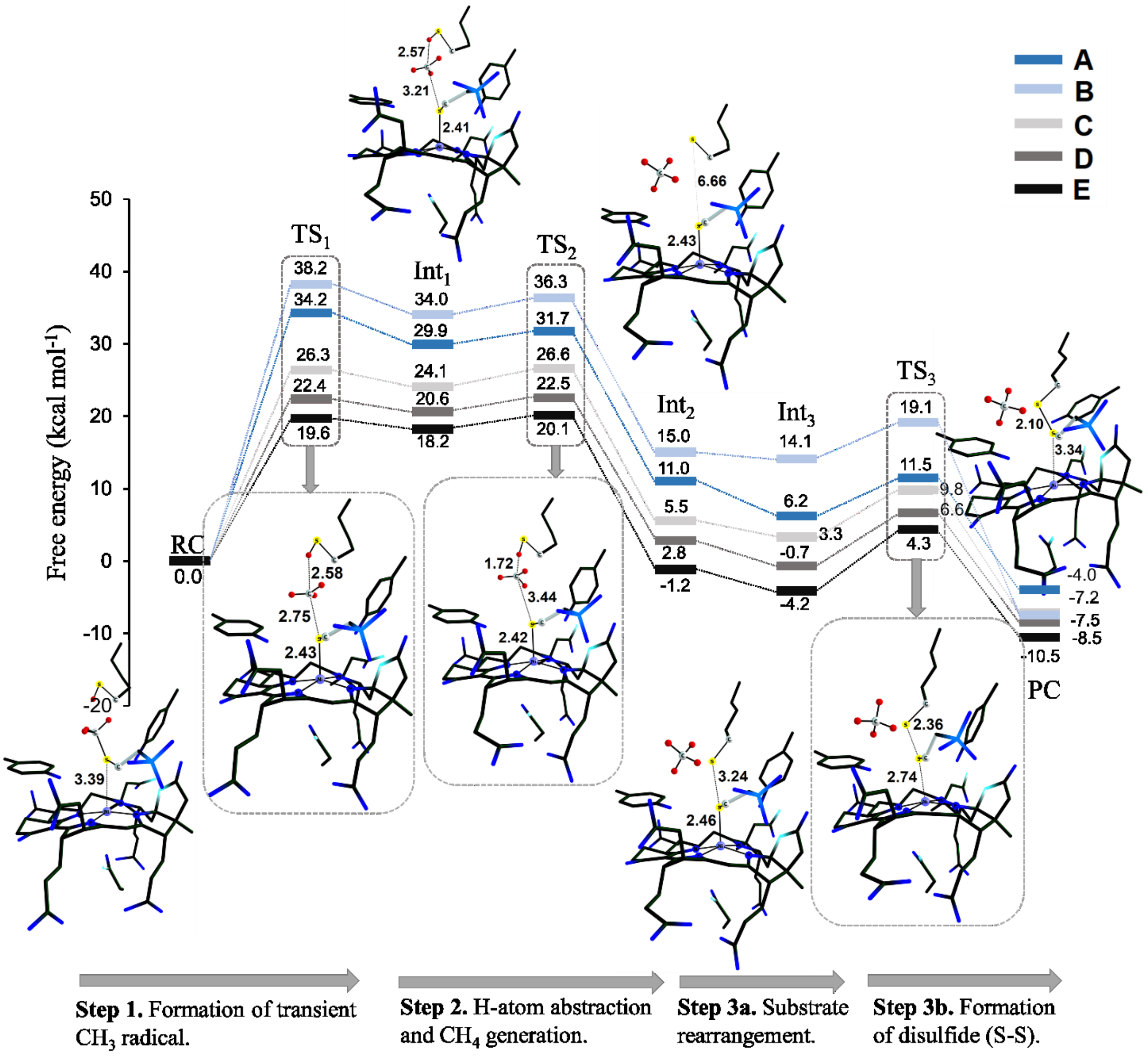

**Figure 6:** Free-energy profile depicting catalyzed methanogenesis within enzyme-like models. Here, **E** denotes the model representing MCR with the native F430, while **A–D** accommodate biosynthetic precursors of F430. To enhance clarity, all critical structures along the catalytic reaction coordinate are shown for model **E**, with only key visualized hydrogen atoms.

by a ballistic trajectory of $CH_3$ towards the crucial H−S bond of coenzyme B, paving the way for direct methane production after traversing $TS_1$. I hypothesize that the extremely pro-reactive movement of $CH_3$ radical towards the S–H bond could avert the buildup of the radical intermediate, posing a potential risk to the integrity and functionality of the protein structure. Interestingly, in the previous study carried out by Siegbahn and coworkers[44], reported the similar observation, *i.e.* a single transition state ($TS_1$) is responsible for methane production with a barrier less **step 2**. Therefore, I would like to conclude that in any case the methyl radical is very short-lived moiety.

In the second step starting from $Int_1$ (**step 2**, **Figure 6**), the associated transient methyl radical captures the hydrogen atom from coenzyme B through the second transition state ($TS_2$) to form $CH_4$ and the intermediate $Int_2$. Note that, for all the models, the energetics for this step is practically unaffected by the chemical environment of the Ni cofactor. The transition state associated with the free-energy barrier ($\Delta G_2^{\neq}$) of **step 2** is only ~2 kcal mol$^{-1}$ higher in energy than $Int_1$, while the free-energy change ($\Delta G_{0,2}$) of this reaction step is found to be exergonic ($\approx -19$ kcal mol$^{-1}$). The low barrier of this step might suggest that the shallow $Int_1$ intermediate can be circumvented through a ballistic trajectory starting from $TS_1$ such that the $CH_3$ radical immediately captures H atom from the key S–H bond of the substrate CoB–SH.

In **step 3**, the CoBS$^{\bullet}$ radical forms bond with the Ni$^{II}$-coordinated thiolate of CoM, resulting in the formation of a disulfide anion radical in $Int_3$ (**step 3a**, **Figure 6**). **Step 3** can be divided into two distinct stages: (*i*) translocation of the substrate radical CoBS$^{\bullet}$ towards the proximity of SCoM in **step 3a** and (*ii*) S–S bond formation along with simultaneous dissociation of SCoM from Ni$^{II}$ (**step 3b**). Regarding the **step 3a**, the movement of the CoBS$^{\bullet}$ radical towards SCoM during the formation of $Int_3$ from $Int_2$ is exergonic in all models **A**–**E**. The establishment of disulfide bond in **step 3b** necessitates to overcoming a barrier ($\Delta G_3^{\neq}$) through $TS_3$. I obtained the highest and lowest value of $\Delta G_3^{\neq}$ for this step for native F430-containing model **E** (8.5 kcal mol$^{-1}$) and **B** (5 kcal mol$^{-1}$), respectively. Interestingly, the variation of $\Delta G_3^{\neq}$ across the **A**–**E** set is smaller as compared to the variation of $\Delta G_1^{\neq}$ in case of rate-determining **step 1**. The energetics of **step 3b** is largely driven by the affinity of electron acceptance ability of Ni$^{II}$ from the corresponding SCoM moiety. Finally, the CoBS–SCoM product formation is accompanied by the dissociation of S–CoM from Ni center.

To conclude this section, I showed that the involvement of any of the investigated Ni-containing cofactors in the reaction between $CH_3$–SCoM and CoB–SH remarkably lowers the activation energy barrier in comparison to the uncatalyzed reaction (**Figures 5** and **6**). This study shows that this type of reaction without the presence of a catalyst is completely unrealistic. Nevertheless, we conclude that the early-stage biosynthetic precursors embedded in models **A** and **B** are still exhibited exceedingly high barriers ($\Delta G_1^{\neq} =$ ~38 and ~34 kcal mol$^{-1}$ respectively). On the other hand, the corresponding two late-stage precursors embedded in models **C** and **D** are associated with much lower barriers. Despite this, **C** and **D** are still inefficient catalysts because their rate-determining barriers, which are 3 and 7 kcal mol$^{-1}$ higher as compared to model **E** with the native cofactor F430.

The above analysis strongly suggests that the most efficient catalyst designed by nature is the native F430-containing active site **E**. It should be noted here that the experimental barrier for methane generation by MCR is 13.2 kcal mol$^{-1}$ as reported by Ragsdale et al.[51] The difference between the experimental and the calculated value lies in one fact. Whereas the carboxylate residues located at the outer edges of the macrocyclic Ni cofactors within the set of models **A**–**E** were considered in the protonated form, these groups are in fact charged in MCR. Therefore, I also assessed the effect of electrostatic impact of these charged residues on $\Delta G_1^{\neq}$ and $\Delta G_{0,1}$ throughout the series **A**−**E**. Interestingly, I observed that in case of both $\Delta G_1^{\neq}$ and $\Delta G_{0,1}$, there exhibit a consistent downward shift of approximately 5 kcal mol$^{-1}$ for **A**–**E**. The calculated $\Delta G_1^{\neq}$ value for **E** is now ~14 kcal mol$^{-1}$, which is close to the experimentally examined one (13.2 kcal mol$^{-1}$). Thus, the role of charged carboxylate groups at the periphery of the corphinoid in F430 is very likely twofold: they contribute significantly to the lowering of the rate-determining barrier, but they also serve as anchors for the macrocycle in the MCR. This finding also indicates that electrostatic effect does not alter reactivity profile across the reaction coordinate between F430 and its precursors, as witnessed by a linear relationship between their charged and neutral form.

## 5.4. Reactivity factor analysis of the rate determining step for A–E (step 1)

In order to understand the key factors that play a major role in determining the energetics of the rate-determining step for **A**–**E**, it is necessary to investigate **step 1** in detail. This includes the construction of a thermodynamic cycle that involves three key events associated with **step 1** from **Figure 6**. Namely, I decomposed the **step 1** into three consecutive events as shown in **Figure 7**. The initial event in the cycle is the homolytic rupture of the S–$CH_3$ bond and the energetics of this step is not influenced by the chemical environment of the Ni macrocycle ($\Delta G'_{cleavage}$, *right upper graph*). The second event corresponds to the electron transfer (ET) from Ni$^{I}$ porphyrin framework to the thiyl group, which eventually form a thiolate anion ($\Delta G'_{ET}$). Finally, the cycle includes the third event, which is Ni$^{II}$–thiolate bond formation ($\Delta G'_{NiS}$). In contrast to the first event, the second and third events are strongly affected by the Ni macrocycle properties. The total free energy of the reaction ($\Delta G'_{0,1}$) from **Figure 7** is given as the sum of each individual terms associated in each event *i.e.* $\Delta G'_{0,1} = \Delta G'_{cleavage} + \Delta G'_{ET} + \Delta G'_{NiS}$. The decomposition of **step 1** into three distinct components is thermodynamically reasonable, as demonstrated by the observed one-to-one correlation (correlation slope reaches nearly to the ideal value of 1, in **Figure 7**, *left graph*) between the free energy of reaction in **step 1** ($\Delta G_{0,1}$) and $\Delta G'_{0,1}$. The two important contributions, $\Delta G'_{ET}$ and $\Delta G'_{NiS}$ to $\Delta G'_{0,1}$ are analyzed in detail in two following sections:

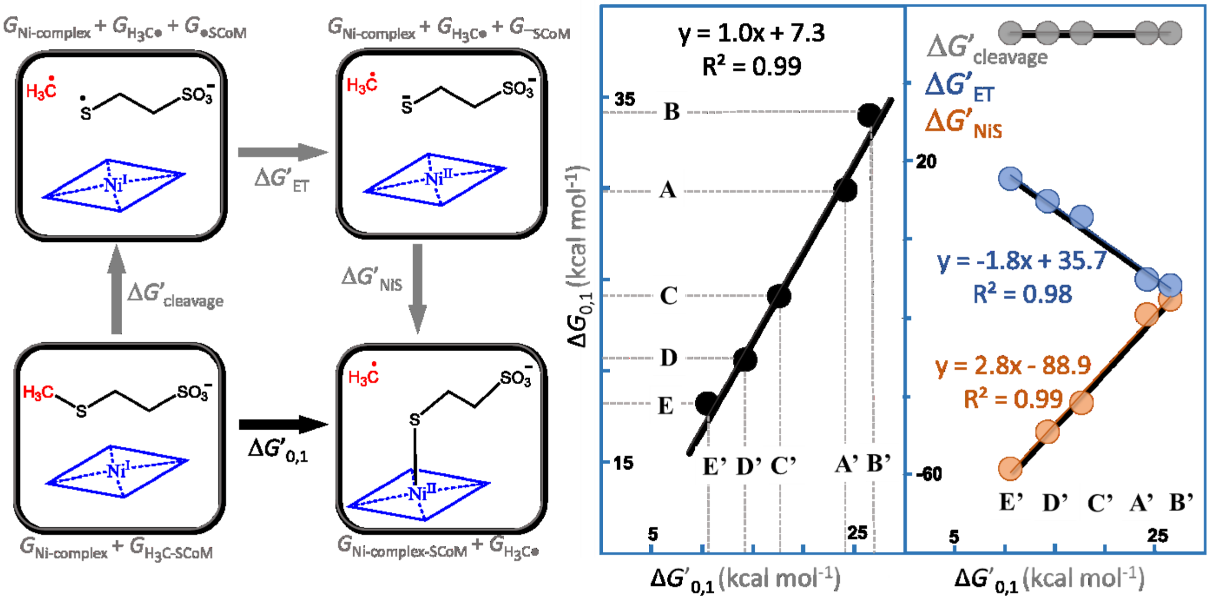

**Figure 7:** Thermodynamic cycle illustrating the initial catalytic step (rate-determining), entailing the generation of the transient methyl radical alongside the one-electron oxidation of the $\text{Ni}^{\text{I}}$ center and the formation of the Ni–thiolate bond. Note that $\Delta G'$ values were evaluated from Gibbs free energies of individual species, as indicated in the figure and using eq 18; the sum of three sequential $\Delta G'$s events equals to $\Delta G'_{0,1}$, which is equivalent to the free energy of reaction ($\Delta G_{0,1}$) from **Figure 6**. The labels **A'**, **B'**, **C'**, **D'** and **E'** are employed in conjunction with the labels for the complete models **A**–**E**. The "prime" symbol indicates that the model comprises separated (infinitely separated) moieties such as the $\text{Ni}^{\text{I/II}}$-complex, $\text{H}_3\text{C–SCoM}$, $^{-/\bullet}\text{SCoM}$, $\text{CH}_3^{\bullet}$, the $\text{Ni}^{\text{II}}$–SCoM complex. Overall, the change in $\Delta G'_{NiS}$. controls the change in $\Delta G'_{0,1}$ and outcompetes the unfavorable change in $\Delta G'_{ET}$ in going from **B'**/**A'** to **E'**.

## 5.4.1. $Ni^{I/II}$ redox potential and its correlation with reactivity in step 1

In this section, I focus on the electron transfer part of the thermodynamic cycle in **Figure 7** ($\Delta G'_{ET}$) with the aim to understand how ET contributes to reactivity. Importantly, the variation of $\Delta G'_{ET}$ across **A**–**E** is given by the difference in reduction potential of Ni macrocycles (as the Ni ion in the key step alters its oxidation state between $Ni^{I/II}$). **Table 1** shows that $E°$ gradually increases as the biosynthetic precursors of F430 gradually approach to F430. This suggests an interesting perspective: the variability of the reduction potential of the Ni center could be a key factor influencing the differences in the free energies of the reaction and in free-energy barriers of **step 1**. In fact, there is an excellent fit correlation between $\Delta G'_{ET}$ and $\Delta G'_{0,1}$, which ultimately correlates with the true free energy of the reaction ($\Delta G_{0,1}$) as shown in **Figure 7** (*right graph, blue*). On closer examination of these findings, however, one observes quite the unexpected result. The observed correlation is totally counterintuitive: a more facile oxidation of the $Ni^I$ center is paradoxically associated with a more endergonic reaction (with a more increase in the value of $\Delta G_{0,1}$). The reductive rupture of the S−$CH_3$ bond is most favorably orchestrated by the native F430 cofactor (anchored in model **E**), despite the fact that F430 is the least proficient in electron donation among other biosynthetic Ni complexes. Therefore, the impact of $E°$ on reaction energetics must be surpassed by another contribution. Such a contribution, which in fact dominates the trend in reactivity across **A**–**E**, is analyzed in the following section.

## 5.4.2. Ni−S bond formation and its correlation with reactivity in step 1

The third factor from thermodynamic cycle (from **Figure 7**) contributing energetics of **step 1** is the $Ni^{II}$–S bond formation ($\Delta G'_{NiS}$). This effect is shown in **Figure 7** (*right graph, orange*). It is evident that the correlation between $\Delta G'_{NiS}$ and $\Delta G'_{0,1}$ witnesses the formation of a stronger $Ni^{II}$–S bond, which eventually leads to a more favorable **step 1**. Model **E** features the strongest $Ni^{II}$–S bond (~-60 kcal $mol^{-1}$), effectively lowering $\Delta G_{0,1}$ as well as the barrier $\Delta G_1^{\neq}$. The calculated correlation slope between $\Delta G'_{NiS}$ and $\Delta G'_{0,1}$ is 2.8, while for $E°$ ($\Delta G'_{ET}$) *vs.* $\Delta G'_{0,1}$ the slope is -1.8 (**Figure 7**). Consequently, the evolution in the Ni−S bond strength across **A**−**E** controls the change in $\Delta G'_{0,1}$, surpassing the counteracting effect of $E°$ by a factor of ~1.5. Therefore, we can directly conclude that the factor that wins over the unfavorable oxidation of $Ni^I$ is the bond formation between $Ni^{II}$ and thiolate. It is the driving factor that dominates reactivity. The overall effect from both $\Delta G'_{NiS}$ and $\Delta G'_{ET}$ quantitatively explains the variation observed in the free energy profile of **step 1** within the **A**–**E** set in **Figure 6**. My results strongly suggest that the impetus for F430 biosynthesis is an adaptation of the Ni electronic structure that strategically lowers the barrier to methane production by strengthening the Ni–S bond formed during the key catalytic **step 1**.

## 5.5. Molecular orbital analysis for step 1

To connect energetics of **step 1** with electronic-structure properties of Ni-containing cofactor, I first constructed and analyzed the representative molecular orbital (MO) diagram for the Ni–S bond formation in going from the initial reactant complex (RC) to $Int_1$ for model **E** (**Figure 8**; model **E** used as reference). The depicted MO diagram features a three-center four-electron interaction between bonding and antibonding orbitals of coenzyme M ($\sigma_{S-CH_3}$ and $\sigma^*_{S-CH_3}$) and Ni-$d_{z^2}$ orbital. The detailed analysis suggests a substantial covalent nature for the Ni−S bond in **E**, and highlights a distinct thiyl character on S. On the other hand, the Ni−S bond in **B**, calculated as the weakest among the set **A**–**E**, is discernibly less covalent, also supported by the diminished Ni and S character on α-$\sigma_{Ni-S}$ and β-$\sigma_{Ni-S}$ orbital, respectively (**Figure 8**). Hence, I would like to highlight our finding that the most pronounced electron donation from thiolate to Ni in $Int_1$ is observed for model **E**, which indicates that the native corphinoid ligand serves as a less potent electron donor in comparison to its biosynthetic macrocycles (**A**–**D**). This is further evidenced by the AIM-charge analysis.

The electron-donation capacity of the macrocyclic ligands in **A**–**E** was evaluated through AIM formalism of the DFT-calculated electron density of their RC complexes (from **Figure 6**). For this purpose, I substituted Ni atom with a point charge ($q_{\mathrm{p}}$) ranging in value from 0e to +1e in increments of 0.1e. It estimates ligand polarization $P(q_{\mathrm{p}})$ as $q_{\mathrm{p}}$ increases. From this, I observed that the behavior of $P(q_{\mathrm{p}})$ varies in a linear pattern across the series **A**−**E**, with the macrocyclic ligand in **A** displaying the highest sensitivity to the incremental increase of $q_p$, while such polarization gradually gets less responsive in model **E**. This suggest that, corphinoid ligand in **E** is finely adjusted to exhibit the least sensitivity to the electric charge of the coordinated Ni ion,

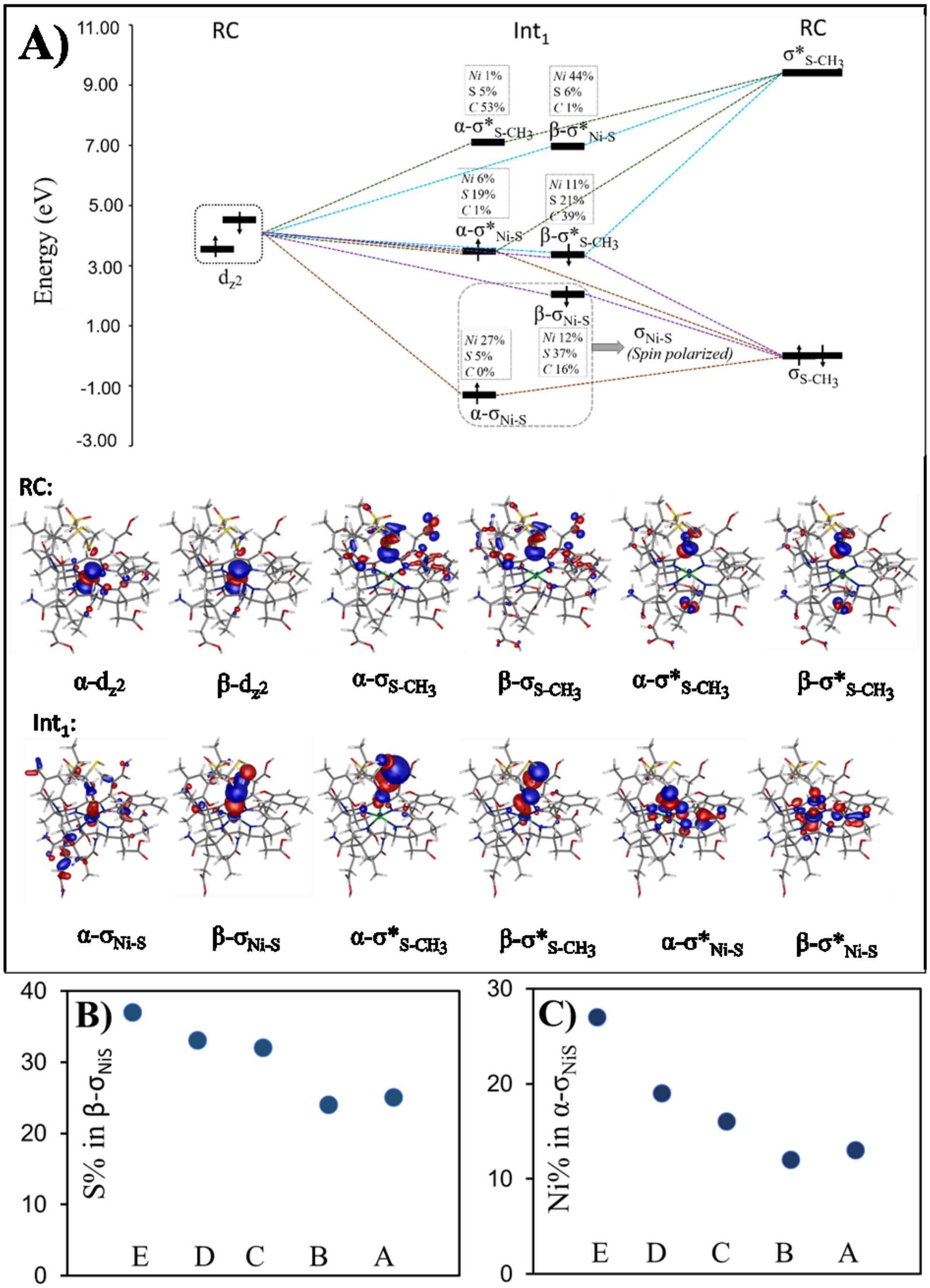

**Figure 8: (A)** Representative MO diagram and molecular orbitals for **step 1** going from RC to Int₁ as illustrated for model **E**. MO energies are shown with respect to the $\sigma_{\mathrm{S-CH_3}}$ energy, which serves as a reference value of 0 eV. The change in the atomic composition in molecular orbitals for Ni–S bond formation is also shown. **(B)** Thiyl character on S in β-$\sigma_{\mathrm{Ni-S}}$ for **A**–**E**. **(C)** Ni character in α-$\sigma_{\mathrm{Ni-S}}$ for **A**–**E**.

followed by the observed trend for the Ni–S bond strength (**Figure 7**). The observed variation in ligand polarizability is instinctively comprehensible, considering that the non-native precursor **A** possesses the most extensive $\pi$-delocalization system, which progressively becomes more saturated as it approaches towards native **E**. Further, I analyzed the nature of bonding between $Ni^{II}$ and the corphinoid ligand in **A**–**E** through AIM-calculated atomic charges ($q_{AIM}$), which provided a straightforward assessment of differential interaction strengths and delocalization indices as a measure of electron sharing. Interestingly, I found that the averaged $q_{AIM}^{N}$ of the four ligating N atoms is the least and the most negative for **E** and **A**, respectively. On the other hand, $q_{AIM}$ for the corresponding Ni centers progressively becomes more positive when retracing the biosynthetic pathway. This result demonstrates that the ligating N atoms in **E** possesses the lowest electron density to delocalize into the Ni center, which facilitates the formation of the strongest Ni–S bond. This electrostatic analysis is also in agreement with the change in corresponding Ni–N and Ni–S bond lengths and bond order as represented in **Figure 9**. I obtained the shortest Ni–S and longest Ni–N bond distances for **E** and that for non-native cofactor **B** vice versa.

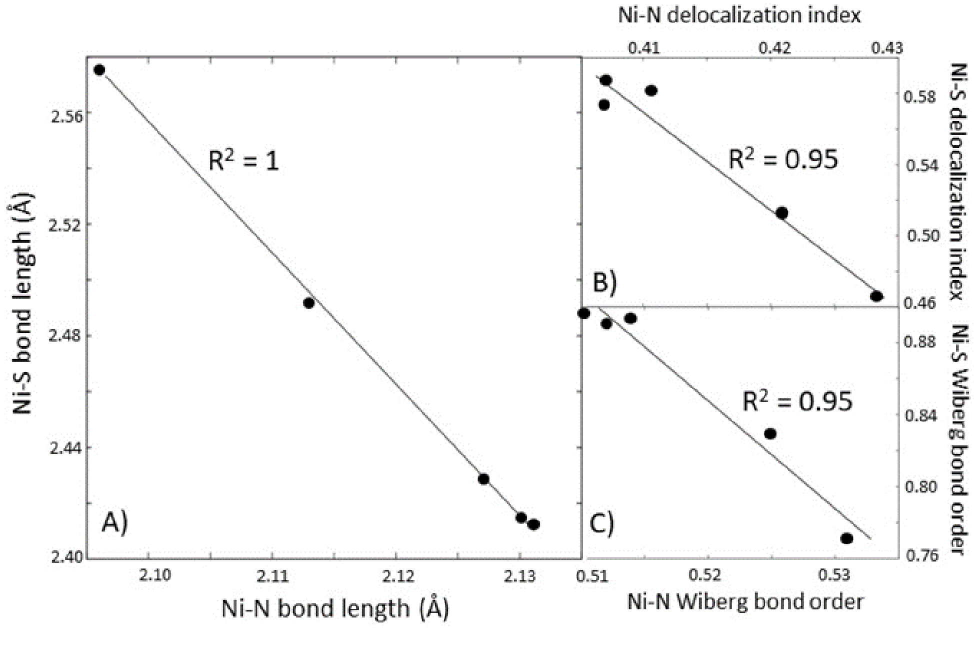

**Figure 9:** Correlation plots between the average length of the four N atoms to Ni and Ni−SCoM bond length (panel **A**); between the Ni−S and average Ni−N delocalization indices (panel **B**); and between the Ni−S and average Ni−N bond (Wiberg bond order, panel **C**).

## 5.6. Connection between kinetic energy distribution (KED) in step 1 and macrocycle electron-donation ability

Along the reaction coordinate of **step 1**, a $\beta$-electron from Ni-$d_{z^2}$ shifts to the unoccupied antibonding $\sigma^*_{\mathrm{S-CH_3}}$ orbital, responsible for diminishing the strength of the corresponding S–CH$_3$ bond. The electronic transition is actually accomplished at TS$_1$, resulting in the rupture of the S–CH$_3$ bond. At TS$_1$, kinetic energy within the reactive mode is mostly concentrated on the transient methyl radical with KED$_{\mathrm{CH_3}}$ to follow the trend **E** (0.882) > **D** (0.862) > **C** (0.859) > **A** (0.790) > **B** (0.788). In both TS$_1$ and Int$_1$, the β-$\sigma^*_{\mathrm{S-CH_3}}$ orbital is singly occupied and maintains the antibonding character between $p_S$ and $p_C$ atomic orbitals ($\sim 19\ vs\ \sim 43\%$ for Int$_1$ in model **E**). Considering these two components, I derived the fraction of $p_C$ presents in $\sigma^*_{\mathrm{S-CH_3}}$ orbital relative to the $p_S$ as $F_{CH_3} = (p_C[\%]/(p_C[\%] + p_S[\%]))$. The computed values of $\mathrm{F_{CH_3}}$ fall within the range of ~0.6–0.7 across set **A**–**E** exhibit an excellent correlation with the corresponding KED$_{\mathrm{CH_3}}$ values, which fall within the range of ~0.8–0.9 (as shown in **Figure 10)**. The increased asymmetry in

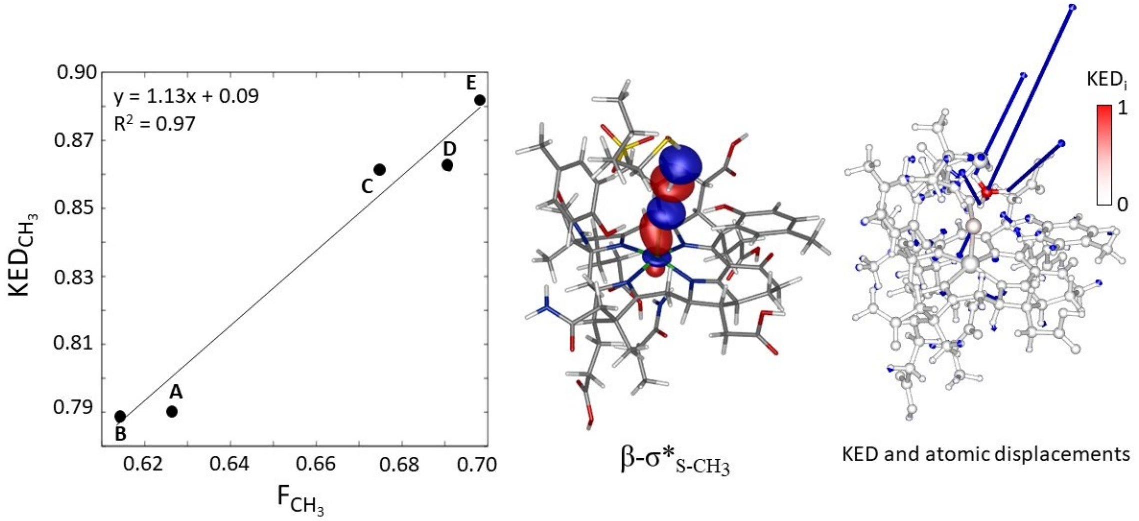

**Figure 10:** Correlation plot of fraction of kinetic energy of the reactive mode from the CH$_3$ radical (KED$_{\mathrm{CH_3}}$) *vs.* fraction of the atomic $\mathrm{p_C}$ orbital in $\sigma^*_{\mathrm{S-CH_3}}$ relative to the atomic $\mathrm{p_S}$ orbital ($\mathrm{F_{CH_3}}$) for **A**–**E**, where $\mathrm{F_{CH_3}}$ evaluated as ($\mathrm{p_C}$[%] / ($\mathrm{p_C}$[%] + $\mathrm{p_S}$[%])), (*left*). Relevant β-$\sigma^*_{\mathrm{S-CH_3}}$orbital for the key S–CH$_3$ breakage step are also showing, related (*center*). Mapping of KED and atomic displacements in the reactive mode of the S–CH$_3$ cleavage step are shown in the right part.

$\beta\text{-}\sigma^*_{S-CH_3}$ orbital favoring the $CH_3$ group leads to a higher KED on $CH_3$. Since the larger asymmetry in $\beta\text{-}\sigma^*_{S-CH_3}$ directly connects with a larger asymmetry in $\beta\text{-}\sigma_{Ni-S}$ in favor of the S character that, in turn, connects with a larger asymmetry in $\alpha\text{-}\sigma_{Ni-S}$ in favor of the Ni component (as discussed earlier). The magnitude and variation of $KED_{CH_3}$ across models **A−E** must then stem from the covalency of the Ni−S bond, which in turn depends on the electron-donation capability of the corphinoid ligand.

## 5.7. Summary of Project I

In summary, I explored the uniqueness of F430 in its ability to facilitate methanogenesis, contrasting it with four consecutively identified precursors formed during its biosynthesis (**Figure 2**) and I found a key factor behind its distinctive role. Namely, I found that none of the precursors reach the proficiency of the native F430, and the catalytic competence progressively enhances with each successive biosynthetic step towards maturation of F430. Contrary to the expected role of F430 as an optimally strong reductant to accelerate the rate-determining reductive cleavage of $H_3C-S$ by $Ni^I$, my findings revealed the opposite outcome. I found that the unfavorable rise in reduction potential along the F430 biosynthetic pathway is counterbalanced by the reinforcement of the Ni−S bond formed during the reductive cleavage of the $H_3C-S$ bond. F430 (**E**) is found to be the weakest electron donor among the four bio-precursors (**A**–**D**), appealing as the most covalent formation of Ni–S bond, which consequently provides sufficient stabilization of the transition state and hence lowering the rate-determining barrier in the key **step 1** (**Figure 6**). Therefore, I present a plausible perspective on how the evolutionary driving force has influenced the biocatalytic efficiency of F430 in methane formation.

## 6. Essential results of Project II:

Traditional TST states that the kinetic ratio of concurrent reactions originating from the same reactants is governed by the difference in free energies of their respective transition states. After that, the dominant product ratios can be quantified from the reaction with the lowest activation energy barrier.[144-145] However, apart these, there is a growing number of reactions, which are displaying non-statistical (non-TST) behavior and for which the traditional TST is no longer applicable.[20-22] Such reactions include the prototypical bifurcating organic reactions, in which the reaction channels diverge after passing a common transition state ($TS_1$ - also known as an ambimodal transition state) and leading to two different products as illustrated by **Scheme 1**.[57-62,146-149] After passing $TS_1$, the potential energy surface is characterized by a valley-ridge inflection point. This point marks the beginning of two different product channels that can be accessed without any additional transition states. Therefore, the related products have no obvious barriers that can be calculated. In fact, the selectivity is solely determined by the atomic positions and momenta of the reactive system after the $TS_1$ configuration has been surpassed. The final branching product ratio is determined by the overlap of these structural and dynamic signatures with the energetically downhill reactive channels.

Numerous pericyclic reactions are considered paradigmatic in the area of bifurcating reactions.[145] Apart from wide variety of organic reactions, the library of bifurcating reactions can be extended to nucleophile substitution *vs*. addition in α-haloketones,[52] Beckmann and Schmidt rearrangements *vs*. fragmentation, and isomeric Pummerer rearrangements.[53] The presence of bifurcations is also observed in metal-catalyzed reactions such as Rh-carbenoid C−H insertions, gold-catalyzed cyclization, asynchronous nitrene insertions, and natural product biosynthesis catalyzed by enzymes.[61,54-56] In this thesis, I cover a variety of well reported bifurcating reactions and I study them under RMCF-based approach (RMCF itself was introduced earlier in the text, section 4.2.). The RMCF-calculated product ratios of all reactions considered in **Project II** were compared with either experimental data or MD trajectory studies, known from literature.

The product selectivity of bifurcating reactions can be explored from both experimental and theoretical perspectives. However, the accurate prediction and quantification of product selectivity from computational approach is still challenging. Till date, only a few computational methodologies are reported that can be used to determine product selectivity of such reactions

(**Figure 11**). A brief introduction of these approaches is given below. The most common traditional approach employs ab initio molecular dynamics (MD) simulations to study reaction dynamics starting from the rate-limiting $TS_1$.[63-64,150-158] The atomic velocities along the direction of $TS_1$ are arbitrarily initialized and the trajectories that result from these initial conditions lead to one of the possible products. This approach demands a collection of a statistically sufficient number of trajectories to reproduce the experimentally determined product ratios. Although ab initio MD can be considered as a powerful tool for making accurate predictions, its main challenge relies on very expensive computational demanding. On the other hand, Carpenter et al. developed a much cheaper computational approach called the "dynamic match" which only requires three stationary points ($TS_1$, $P_A$, and $P_B$) on the potential energy surface illustrated in **Scheme 1**.[69] This method projects the imaginary eigenvector of $TS_1$ onto two post-$TS_1$ reaction coordinates of two distinct pathways. However, only a few reactions have been investigated using this method, so I later tested the effectiveness of this approach on a larger scale for the range of bifurcating reactions considered in **Project II**. Another comparatively cheaper method than ab initio MD was described in the group of Houk.[65] Such a method is based on differences of bond orders in $TS_1$, which are directly linked to the formation of two distinct products.[66-68] This method is completely empirical. Very recently, Goodman et al develop an algorithm that predicts the major products in bifurcating organic reactions with low computational cost.[70-71] Their approach takes the geometries and the imaginary eigenvectors of the two transition states ($TS_1$ and $TS_2$) and the two products ($P_1$ and $P_2$) as inputs. Their algorithm predicts the product selectivity of the bifurcating reactions by estimating the topology of the potential energy surface. Summarizing all the existing computational protocols apart from MD, I note that the dynamic match approach, Goodman's approach and Houk's bond-order method can be recalled accordingly as three-point, four-point and one-point method, respectively (**Figure 11**), as their numerical solution depends on the specified number of structures to be considered.

The approach developed in our laboratory predicts the branching product selectivity based on requirement of only one key point $TS_1$ from the PES (as shown in **Scheme 1**). The method I demonstrate in this thesis relies on the kinetic energy distribution within the reactive mode at $TS_1$, which might be applicable in a broader perspective way with no limitation to reactions with 'four-point'-defined furcations and/or without bias towards pre-defined products. In section 4.2., I discussed the theory of our method which we denoted as reactive mode composition factor

(RMCF) analysis. In the upcoming discussion part of the thesis, I studied the accuracy of RMCF approach (section 6.3. and 6.4.) in prediction of branching product ratios for the wide variety of bifurcating reactions. Also, I provide a comprehensive analysis of its competitiveness with existing computational protocols, as introduced above (*cf.* **Figure 11**). Finally, I briefly summarize the limitations of RMCF analysis (section 6.5.).

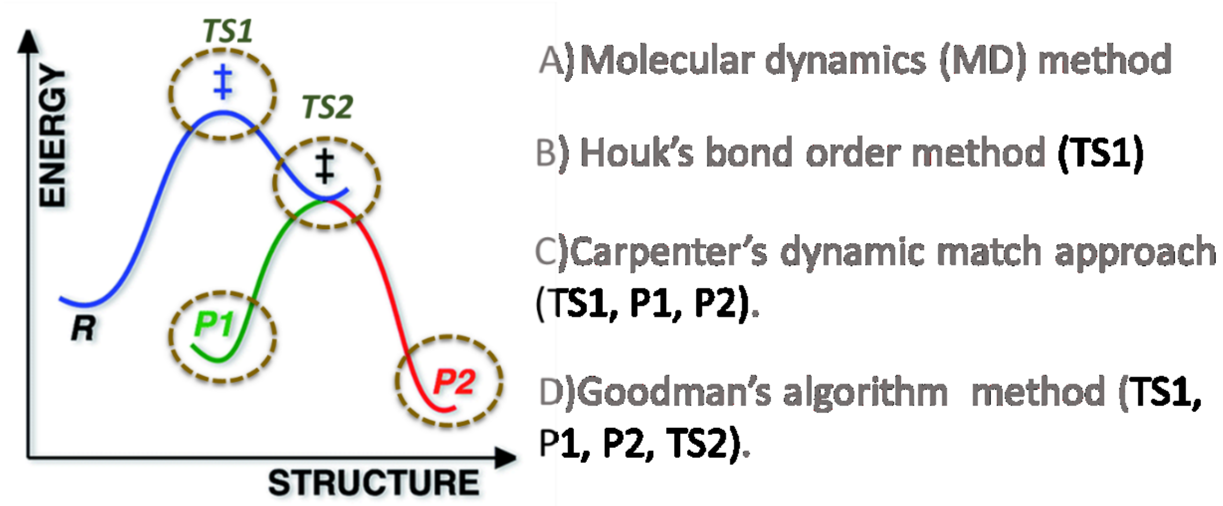

**Figure 11:** Existing method employed for predicting bifurcating product ratios.

## 6.1. Application of RMCF analysis in predicting bifurcating product ratios

A challenging task in the prediction of the various product ratios by KED is to determine the appropriate number of atoms directly involved in the formation of the various branching products. Thus, the approach involves grouping the atomic KED factors into such *N* sets responsible to *N* different reactive channel. The $TS_1$ reactive mode is then divided into *N* fractions, each of which is available to one of the reactive channels. For example, in case of two competing post-$TS_1$ reactive channels A and B, it is necessary to make two individual disjunctive groups of atoms and calculate their $\mathrm{KED}_{\mathrm{RM}}$ (KED of the reactive mode, $\mathrm{KED}_{\mathrm{RM}}$) factors at $TS_1$ reactive mode as $\mathrm{KED}_A(=\sum_{j=1}^{p}\mathrm{KED}_{j,\mathrm{RM}})$ and $\mathrm{KED}_B(=\sum_{i=1}^{p}\mathrm{KED}_{i,\mathrm{RM}})$ respectively (RM: reactive mode). Then, the percentage of either product A or B ($\chi_{KED}(A/B)\%$) can be estimated employing eq 27:

$$\chi_{KED}(A/B)\% = 100 \times \frac{KED_{A/B}}{KED_A + KED_B}$$

$$= 100 \times \frac{\sum_{j=1/i=1}^{p} \mathrm{KED}_{j,\mathrm{RM}/i,\mathrm{RM}}}{\sum_{j=1}^{p} \mathrm{KED}_{j,\mathrm{RM}} + \sum_{i=1}^{p} \mathrm{KED}_{i,\mathrm{RM}}} \qquad (27)$$

Note that eq 27 can be used to calculate product ratios for any $N > 2$ reactive channels.

## 6.2. TS partition for the calculation of branching ratios of bifurcating reactions

In **Project II**, I considered a set of 48 bifurcating reactions to analyze product ratios (**Figure 12**) that were previously investigated computationally by Lee and Goodman.[12] Additionally, I also considered other 13 bifurcating reactions, which I discussed in more detail in section 6.3. (**Figure 15**). The analyzed reactions encompass a wide range of reactions which included a variety of organic pericyclic reactions (**1**–**12**, **23**–**34**, **47**–**48**),[54,61,159-171] nitrene insertion reactions (**35**–**38**),[172] rearrangement and fragmentation reactions (**13**–**16**, **39**),[53,157,173-175] nucleophilic additions and substitutions (**17**–**22**, **46**)[62,175] and solvent-dependent isomeric Pummerer rearrangements (**40**–**44**)[52] reactions, as summarized in **Figure 12**. As reference data, I took advantage of the calculated molecular dynamics (MD) and experimental product ratios for these reactions to assess the reliability of the presented KED-based method.

Regardless of the type of reactions considered, I found a consistent and reliable approach to $TS_1$ partitioning (**Scheme 2A**). Namely, the partitioning (atomic grouping) follows the procedure:

(1) For each of the *N* relevant products, pinpoint the atom pairs that are directly engaged in bond formation or cleavage and assign them to separate groups. Exclude the bonds that are common to all products during the formation or cleavage process.

(2) Consider all the H-atoms that are directly bound to each group.

(4) The remaining atoms present in $TS_1$ are ignored.

On the other hand, for the reactions **13**–**16**, **24** and **52,** only one bond is formed and one is cleaved. For these types of reactions, I provided an alternative approach to calculate product ratios (shown in **Scheme 2B**):

(1) Determine the atom pair responsible for forming the distinct bond, encompassing all directly linked H-atoms within this partition. This fragment aligns with channel A.

(2) Identify the atom pair associated with the breaking or forming of the bond shared by all products. Ensure that all directly bonded H-atoms are included in this group.

(3) Consider fragment B with the rest of atoms that are not associated with fragment A and common fragment.

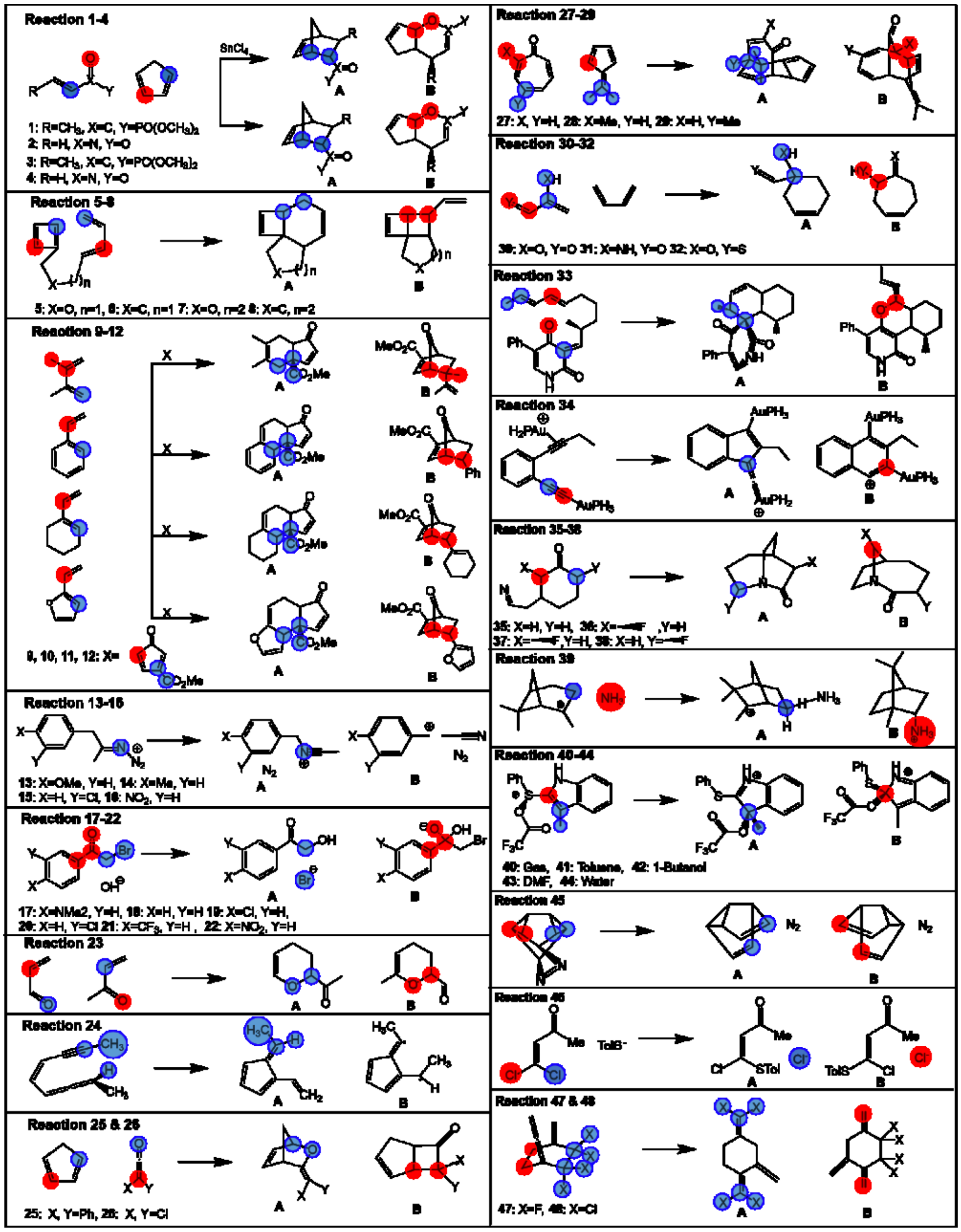

**Figure 12:** Bifurcating reactions considered in **Project II**. Partition of each reactive system for calculation of product ratio ($\chi$) is considered according to the procedure in **Scheme 2**. Blue and red colors correspond to partitions A and B respectively.

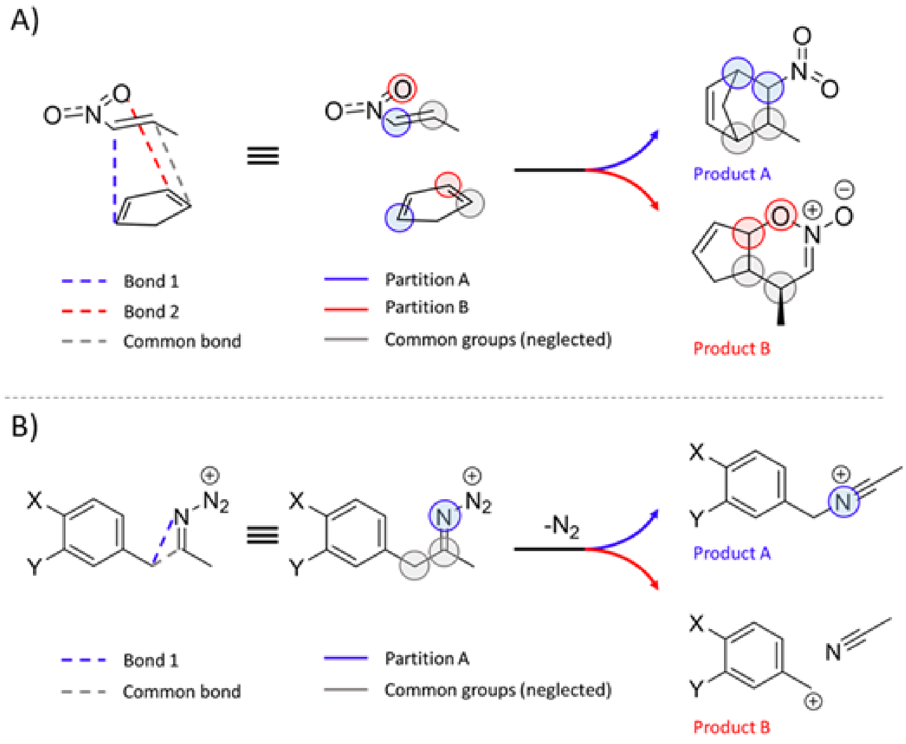

**Scheme 2: A)** Partition of $TS_1$ into two groups of atoms ascribed to two competing channels in bifurcating reactions. Each group is linked to a portion of the kinetic energy from the reactive mode at $TS_1$, which is used to calculate the product branching ratio $\chi_{KED}$ using eq 27. **B)** Partitioning scheme for reactions involving the breaking and the formation of only one bond.

## 6.3. RMCF analysis of transition states from bifurcating reactions

Following the prescription described above in section 6.2. and **Scheme 2** for atomic grouping within $TS_1$, I calculated the KEDs for both fragments A and B for all 48 bifurcating reactions from **Figure 12**. I then plugged $KED_A$ and $KED_B$ into eq 27 to calculate the percentage of the product formation for each reactive channel (**Figure 13**) and then, compared $\chi_{KED}$ with referential experimental and MD data ($\chi_{Ref(Exp/MD),major}$). I found that RMCF successfully predicts the major product up to 89% for 41 reactions out of 46. An inspection of **Figure 13** states that most of the reactions are occupied on the top-right quadrant, which demonstrates that RMCF successfully predicts correct product quantification for majority of the cases. However, we found an exception for reactions **5**, **12**, **15**, **16** and **22**, where RMCF defines minor products contrary to the reference predicted major products. Furthermore, **Figure 13** illustrates that the calculated absolute unsigned deviation from the reference data (referred to as $KED_{error}$) is below 10% for 25 instances and below 20% for 34 out of the 48 reactions. Overall, the RMCF analysis reliably identifies the predominant product in 89% of the examined cases, while achieving accurate quantification (within a tolerance of <20%) in 80% of those instances.

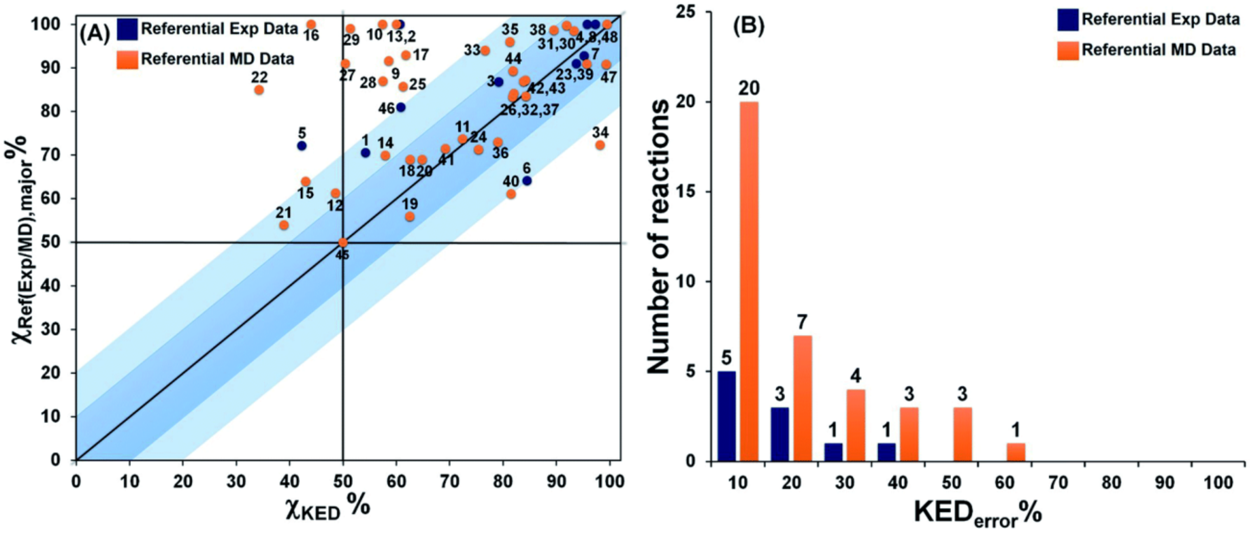

**Figure 13:** The correlation between $\chi_{KED}$ from eq 27 and the referential experimental or MD simulations (*blue* or *orange points*) values, $\chi_{Ref(Exp/MD),major}$ for reactions **1–48** (from **Figure 12**) are shown (panel A). Here $\chi_{KED}$ denotes the calculated major product in the reference. The distribution of reactions according to the unsigned deviation $KED_{error} \equiv |\chi_{KED} - \chi_{ref\,(Exp/MD),\,major}|$ are illustrated in panel B.

After testing the Goodman's set of 48 reactions, I applied our protocol to second set of additional 13 bifurcating reactions, as shown in **Figure 14** and **Figure 15**.[68,56,176-180] Again, our RMCF approach is shown to be robust in handling these ambimodal reactions, accurately predicted product distributions with errors less than 20% in 77% of the examined cases, yielding a mean unsigned error of 14%. This demonstrates the commendable performance of the method in general organic reactions and extends its applicability beyond the dataset used in its development. Reactions **59–61** involving different tropones and cycloheptatriene feature trifurcating potential energy surface, which shares a single $TS_1$ responsible for the formation of three different products. However, molecular dynamics ratio predicts the propensity for the formation of product C as 0%.[68] This led me to consider these reactions as bifurcations that avoid the possibility of the formation of product C. The evaluated product A and B distributions for reactions **59**, **60** and **61** are as follows: 39% : 61% (*vs*. MD ratio 36% : 58% for **59A** : **59B**); 42% : 58% (*vs*. 63% : 30% for **60A** : **60B**), and 36% : 64% (*vs*. 55% : 37% for **61A** : **61B**). The origin of discrepancies for reactions **60** and **61** might be attributed to the presence of steric hindrance in them, which is in accord with the Houk's original explanation.[68]

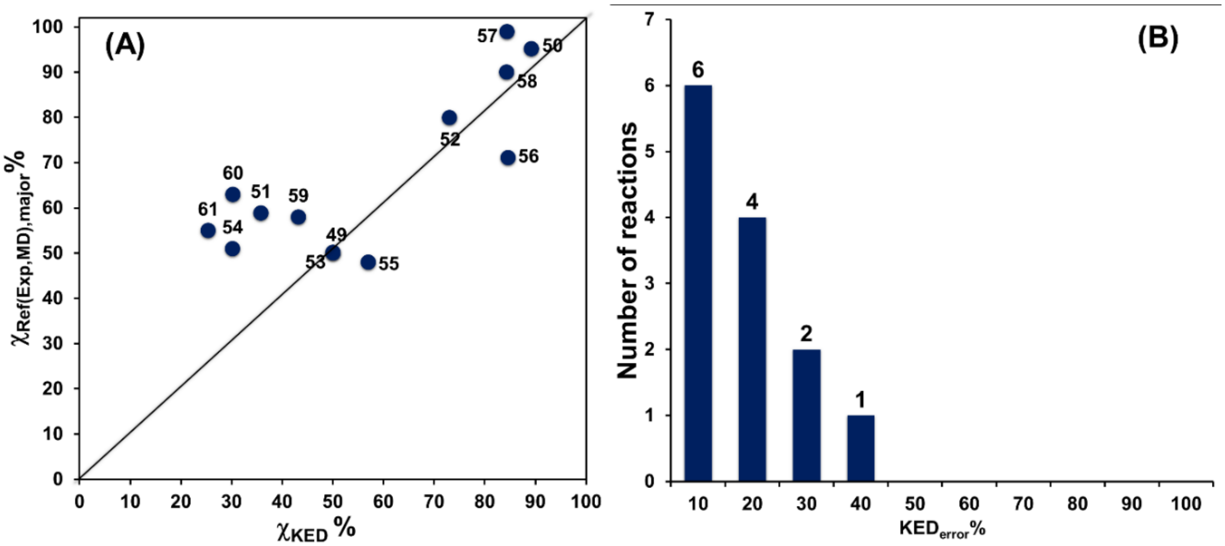

**Figure 14:** The correlation between $\chi_{KED}$ and the referential $\chi_{Ref(Exp,MD),major}$ values, as obtained from MD simulations for reactions **49–61** (panel A). Note that $\chi_{KED}$ refers to the product that is determined as a major product in the reference. The distribution of the number of reactions according to the unsigned deviation $KED_{error} \equiv |\chi_{KED} - \chi_{Ref(Exp,MD),major}|$ are shown in panel B.

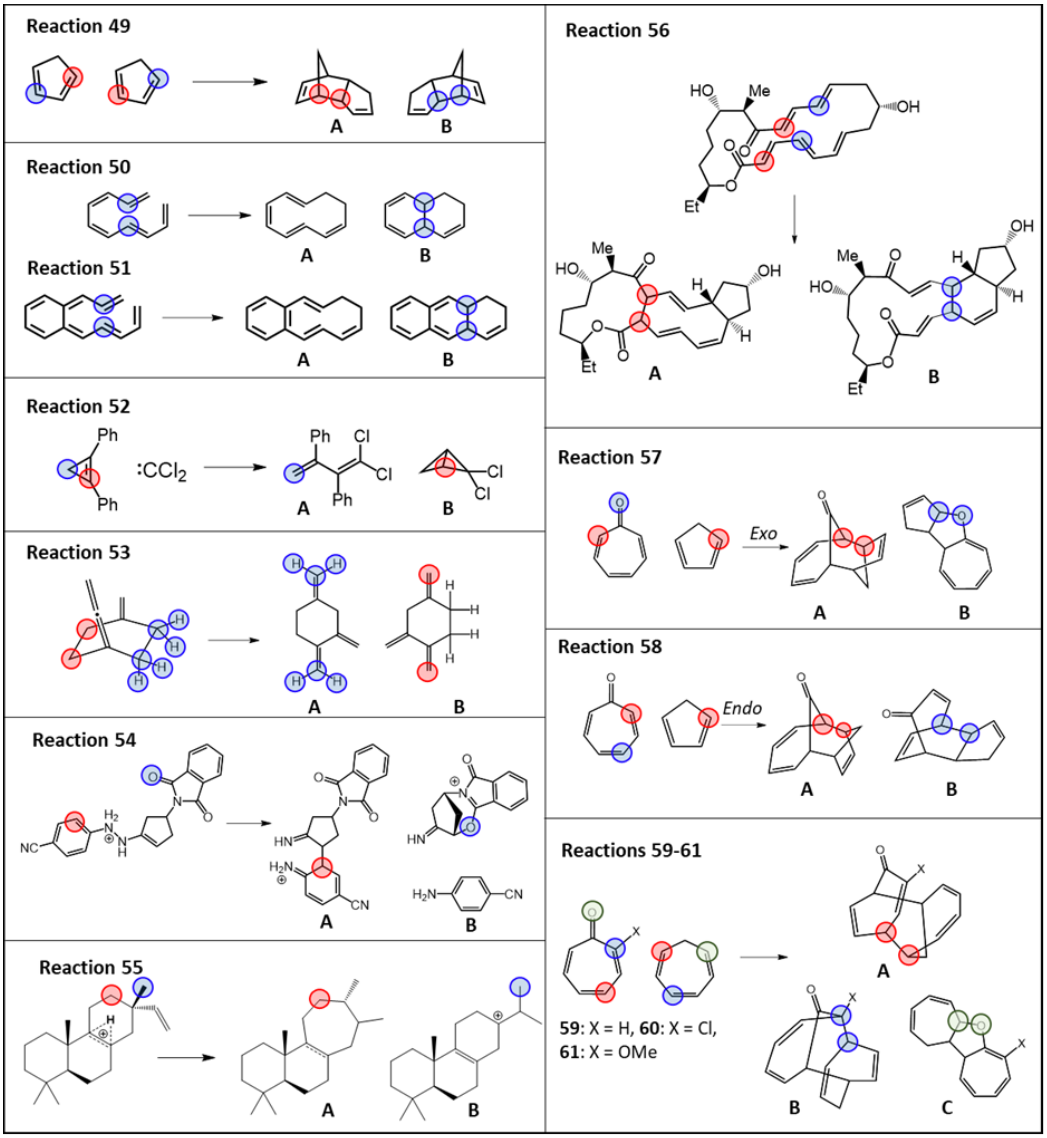

**Figure 15:** Second set of bifurcating reactions considered in **Project II**. Partition of each reactive channel for evaluation of branching ratio (χ) is calculated accordingly as shown in **Scheme 2**. Blue, red and green colors refer partitions A–C, respectively.

## 6.4. Comparison of RMCF product ratio with existing protocols

In this section, I discuss the performance of RMCF-based approach as compared to other three existing protocols from **Figure 11**. An inspection of product outcomes by Goodman's method, I obtained 81% of correct major product selectivity with calculated errors less than 10% for 53% and below 20% for 71% cases (**Figure 16**). I note that reactions **15**, **16** and, **34** after many attempts I could not able to locate $TS_{AB}$. Therefore, under the perspective of stringent prerequisite of all four optimized structures, Goodman's method might limit its suitability for a wider range of reactions. Furthermore, this method proves to be more challenging for multiple branching reactions, such as trifurcating reactions, which require a strict criterion of knowing all 7 stationary points. In contrast, RMCF seems a better tool as it requires only one point from PES and qualitative information of the suspected products. However, a comparison between two approaches quite similar: RMCF predicts qualitatively correct selectivity in 93% (40 out of 43) and with the correct quantification (with a tolerance of 20%) in 71% of cases.

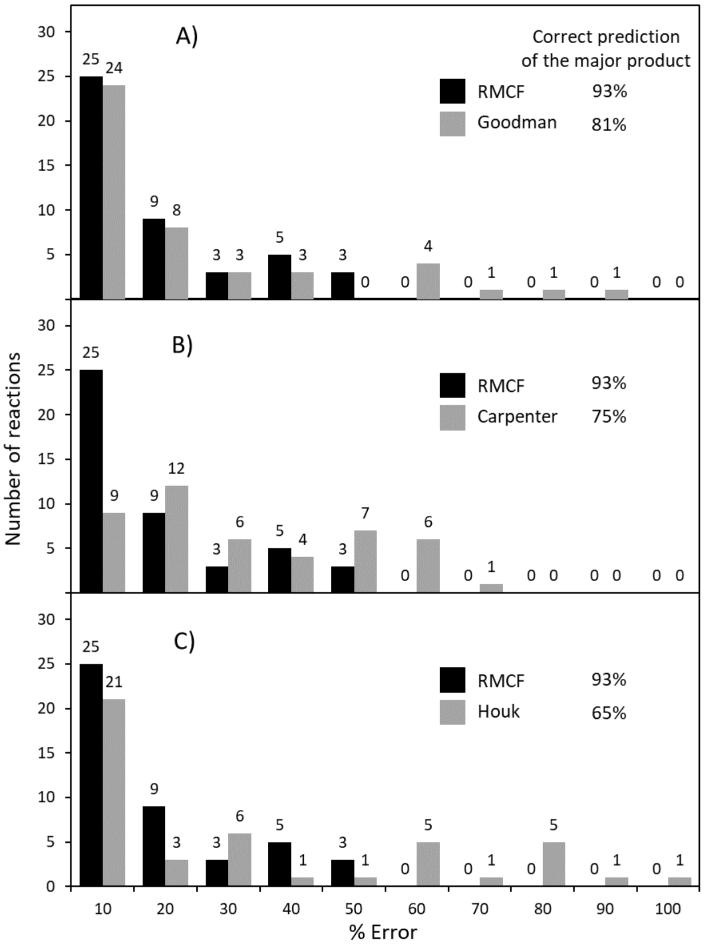

**Figure 16:** The performance of the RMCF method is compared against three other PES-topology-based approaches: Goodman's algorithm (panel A), Carpenter's dynamic match (panel B), and Houk's bond-order-based fitting function (panel C). The performance of these four methods is

evaluated using reference data (either experimental or molecular dynamics) for the reactions displayed in **Figure 12**.

Carpenter's dynamic match predicts the major product for 72% of reactions. However, the dynamic approach is notably less effective for quantification of the product ratio: only 20% (and 47%) of reactions falling within a 10% (and 20%) deviation from the reference data.

Ultimately, Houk's approach for bond order ratios (BOR) at the ambimodal $TS_1$ depends on a linear regression applied to a training dataset of reactions. It is anticipated to perform satisfactorily for processes closely resembling to those within the training data. It correctly identifies the primary product in 67% of cases (**Figure 12**), with 47% (and 54%) of all predicted outcomes falling within a 10% (and 20%) margin of error compared to the reference data.

To sum, RMCF offers the optimal balance between simplicity and accuracy. RMCF is comparatively more advantageous in terms of applicability than Houk's BOR approach, where it demands very minimal requirement, just only a one point ($TS_1$) from the PES. It is also beneficial in terms of quantification than Carpenter dynamic match method as later predicts only with 20% of reactions falling within a 10% deviation from the reference data. Further, when RMCF is supplemented with qualitative information about the anticipated products, its accuracy matches or even exceeds than that of the four-point algorithm proposed by Goodman et al.

## 6.5. Advantages and limitations of RMCF

One-point approaches offer distinct advantages, especially when obtaining additional points on the PES is challenging or computationally expensive. This is especially true when dealing with scenarios where more than two products emerge from $TS_1$. Nevertheless, it must be acknowledged that reactions **5** and **13**–**16** are largely beyond the capabilities of the RMCF and the other three methods tested, highlighting the persistent problem of solving complex trajectories using simplified models. Regarding reaction **5**, the motion observed at the $TS_1$ structure suggests a preference for (4 + 2) cycloaddition, a pathway that is actually less favored. Therefore, it appears that a tight –$CH_2OCH_2$– ether group in the molecule overrides the kinetic energy preference at $TS_1$, ultimately resulting in the (2 + 2) product.

Another unavoidable limitation of our approach arises from the lack of temperature dependence in the RMCF analysis. Though a thermostat is commonly employed in MD simulations to enable the variation of product outcomes with temperature, it's essential to highlight that the eigenvalues of the diagonalized Hessian matrix - and, consequently KED - remain unaffected by temperature changes. However, there is limited evidence to indicate a notable alteration in branching ratios resulting from temperature variations. As an example, the experimentally determined product ratio for the thermolysis of enyne-allenes (a reaction similar to **24**) exhibits a variation in the range of 2–4% as the temperature is elevated from 30° to 100°C.[176] Another relevant example is the activation of $CH_4$ by $MgO^+$, which has been investigated through both experimental studies and molecular dynamics (MD) simulations.[149] Although the calculated potential energy surface (PES) is expected to reveal a shallow intermediate, this reaction does not fit the typical profile of a canonical bifurcating reaction. However, MD trajectories circumvented this intermediate, leading directly to one of two possible reactive pathways, similar to a bifurcating reaction. Notably, only a slight shift in product distribution (3%) occurred as the temperature increased from 300 to 600 K, indicating that dynamically controlled reactions may exhibit relatively low sensitivity to temperature variations, thus amenable to RMCF analysis. Overall, the impact of temperature on the outcome of branching reactions is an area that is not thoroughly explored.

## 6.6. Application to reactions featuring statistical and non-statistical contributions

In certain scenarios, reactions may involve both *statistical* and *non-statistical* steps. Statistical steps can be rationalized using Eyring's transition state theory (TST), while non-statistical steps can be treated by e.g. RMCF analysis. Here, I illustrate the application to such combined reactions to demonstrate the versatility of the RMCF protocol. The first example is the reaction between dichlorocarbene and 2-methylbenzocyclopropene, reaction **62**, as depicted in **Figure 17**.[178] Consistent with the initial reports,[178] I found the presence of two isomeric and closely similar transition states ($\Delta\Delta G^{\neq} = 0.5$ kcal mol$^{-1}$), each capable of bifurcation to produce the isomeric products **62A** and **62B**. Utilizing TST, I calculated a statistical partitioning of $70\% : 30\%$ between the two transition states ($TS_{1A}$ : $TS_{1B}$ from **Figure 17**). Applying RMCF approach, I predicted non-statistical ratios for products **62A** and **62B** as $95\% : 5\%$ (from $TS_{1A}$) and $9\% : 91\%$ (from $TS_{1B}$). Taking together these outcomes, I anticipated a ratio between **62A** and **62B** to be 69% : 31%, matching remarkably well with the experimental ratio of 68% : 32%. Further, I successfully applied this approach for predicting product quantification of challenging tripericyclic reaction between 8,8-dicyanoheptafulvene and 6,6-dimethylfulvene (reaction **63**).[147-149]

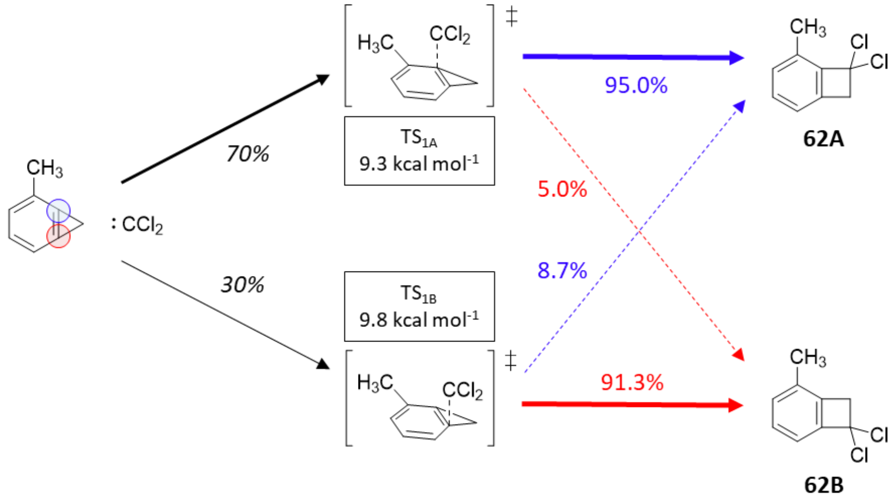

**Figure 17:** Reaction **62**, featuring two energetically close transition state, each of them showcasing a different product channel. Ratios in black were calculated from TST and colored percentages from RMCF approach.

---

## 6.7. Summary of Project II

---

In summary, I discussed the application of our RMCF approach to evaluate bifurcation selectivity by analyzing the energy distribution within the reactive mode of the first transition state. Our method showed remarkable consistency with MD and experimentally reported product ratios and accurately predicts selectivity in 89% of nearly 60 diverse cases, including pericyclic reactions, rearrangements, fragmentations, and metal-catalyzed processes, along with a set of trifurcating reactions. Interestingly, with 71% of product ratios having an error margin of less than 20%, the methodology outperformed three other recent approaches. Given its predictive accuracy, this procedure offers a feasible path for reaction design, even in the context of complex non-TST chemical steps.

## 7. Conclusion:

In the thesis, I described my research on two topics. The common theme of the two topics is chemical reactivity/selectivity - one from the field of metalloenzymology and the other from the field of organic chemistry. The first relies on the use of the standard TST, the second deals with chemical reactivity going beyond TST. The two projects are summarized as follows.

**Project I.** Methanogenesis represents a distinctive form of anaerobic respiration that has been refined by evolution for maximum efficiency. In the terminal phase of this unique metabolic pathway, methane is generated through the reaction between a thiol and a thioether, catalyzed by methyl-coenzyme M reductase. At the heart of this enzyme lies the potent active site housing the Ni-containing F430 cofactor, whose catalytic performance have been scrutinized within the framework of evolutionary forces guiding its biosynthesis.

Here, I leveraged the insights gained from four recently identified biosynthetic precursors of F430, and investigated their reactivity in comparison to the native F430. My findings revealed that F430 is optimally best suited for catalysis, exhibiting the lowest reaction barrier for the rate-determining step involving the reductive breakage of the thioether S–$CH_3$ bond by the $Ni^I$ center. Interestingly, F430 has the highest reduction potential and is therefore the least effective reductant for breaking the S–$CH_3$ bond. However, another crucial factor in favor of native F430 is the strength of the Ni–S bond formed in the reductive cleavage of S–$CH_3$, which actually eliminates the possibility of an inappropriate reduction potential. This bond emerges as the strongest for native active-site models anchoring F430 among its four biosynthetic precursors. The enhanced strength of the Ni–S bond is attributed to the highest covalent character, result of the weakest electron-donation ability of the native porphyrin-like F430 skeleton, a consequence of the complex chemical modifications occurring in the biosynthetic route of F430, particularly in the native porphyrin-like F430 skeleton.

**Project II.** Bifurcating reactions serve as paradigmatic examples, transcending the conventional bounds of Eyring transition state theory (TST). These reactions inherently traverse a common ambimodal transition state ($TS_1$), orchestrating the simultaneous formation of two products. In this thesis, I introduce a protocol that enables the precise quantification of product ratios in bifurcating reactions. This is achieved by partitioning the kinetic energy distribution (KED) of the reactive mode at the shared transition state into chemically meaningful and well-defined fragments. I postulated a theoretical connection between KED and branching ratios, which I validated across a comprehensive set of over 60 bifurcating reactions. The strength of the RMCF analysis becomes apparent when compared to existing computational protocols designed for predicting branching ratios. It consistently outperforms all tested alternatives, excelling in predicting major products. Our method yields comparable results to the most successful method reported to date, requiring only a single transition state connecting the reactant complex with available product channels, supplemented by qualitative information about the bifurcation products. Importantly, the method can be seamlessly integrated with traditional transition state theory, making it applicable to reactions involving sequential TST and non-TST steps. The results show excellent agreement with experimental and molecular dynamics (MD) outcomes, highlighting the versatility and reliability of our approach. In its entirety, the RMCF protocol stands as a versatile and sophisticated approach for the prediction and comprehension of bifurcating and multifurcating reactions. Its excellent ability to flawlessly participate into the analysis of chemical reactions, together with its flexible involvement in TST and accurate quantification of kinetic energy distributions across reaction regimes, positions this method as a user-friendly approach to better understand complex reaction mechanisms.

## 8. List of abbreviations:

| | |
|---|---|
| TST | Transition state theory |
| MCR | Methyl-coenzyme M reductase |
| DFT | Density fuctional theory |
| KED | Kinetic energy distribution |
| PES | Potential energy surface |
| VRI | Valley-ridge inflection |
| MD | Molecular dynamics |
| RMCF | Reactive mode composition factor |
| TS | Transition state |
| CI | Configuration interaction |
| CC | Coupled cluster |
| CASSCF | Complete active space self-consistent field |
| HF | Hartree-Fock |
| KS | Kohn-Sham |
| LDA | Local density approximation |
| GGA | Generalized gradient approximation |
| GTO | Gaussian Type Orbital |
| STO | Slater Type Orbital |
| LCAO | Linear combination of atomic orbital |
| DZ | Double Zeta |
| TZ | Triple Zeta |
| ECP | Effective Core Potential |
| CPCM | Conductor-like polarizable continuum model |
| AIM | Atoms-in-molecules |
| NHE | Normal hydrogen electrode |
| QM/MM | Quantum mechanics/molecular mechanics |
| RR | Reactant region |
| PR | Product region |
| RM | Reactive mode |
| IRC | Intrinsic reaction coordinate |
| RC ` | Reactant complex |
| PC | Product complex |
| MO | Molecular orbital |

## 9. Bibliography:

[1] Laidler, K. J. A lifetime of Transition-State Theory-This is a story of the theory that has provided chemists with a framework for gaining some understanding of even the most complicated chemical reactions. *Chemical Intelligencer*, **1998**, *4* (3), 39-47.

[2] Wigner, E. P., & Eyring, H. On the Rate of Chemical Reactions. In *Part I: Physical Chemistry. Part II: Solid State Physics* ,**1937**, 153-156. Berlin, Heidelberg: Springer Berlin Heidelberg.

[3] Peters, B. Transition state theory. *Reaction Rate Theory and Rare Events Simulations*, **2017**, 227–271.

[4] Eyring, H. The activated complex in chemical reactions. *The Journal of Chemical Physics*, **1935**, *3* (2), 107-115.

[5] Laidler, Keith J., & M. Christine King. "The development of transition-state theory." *J. phys. Chem*., **1983**, *87* (15), 2657-2664.

[6] Ptáček, P., Šoukal, F., & Opravil, T. Introduction to the transition state theory. *Introducing the Effective Mass of Activated Complex and the Discussion on the Wave Function of this Instanton*, **2018**, *27*.

[7] Guengerich, F. P. Mechanisms of cytochrome P450-catalyzed oxidations. *ACS catalysis*, **2018**, *8* (12), 10964-10976.

[8] Dawson, J. The Catalytic Mechanism of Chymotrypsin & Measuring Activity. *BIOC* 2580: Introduction to Biochemistr*y, **2021**.

[9] Stewart, J. J. An investigation into the applicability of the semiempirical method PM7 for modeling the catalytic mechanism in the enzyme chymotrypsin. *J. Mol. Model*., **2017**, *23*, 1-27.

[10] Pantazis, D. A. The S3 state of the oxygen-evolving complex: Overview of spectroscopy and XFEL crystallography with a critical evaluation of early-onset models for O–O bond formation. *Inorganics*, **2019**, *7* (4), 55.

[11] Askerka, M., Wang, J., Brudvig, G. W., & Batista, V. S. Structural changes in the oxygen-evolving complex of photosystem II induced by the S1 to S2 transition: A combined XRD and QM/MM study. *Biochemistry*, **2014**, *53* (44), 6860-6862.

[12] Oertell, K., Chamberlain, B.T., Wu, Y., Ferri, E., Kashemirov, B.A., Beard, W.A., Wilson, S.H., McKenna, C.E., & Goodman, M.F. Transition state in DNA polymerase β catalysis: rate-limiting chemistry altered by base-pair configuration. *Biochemistry*, **2014**, *53* (11), 1842-1848.

[13] Tantillo, D. J. Beyond transition state theory—Non-statistical dynamic effects for organic reactions. *In Advances in Physical Organic Chemistry*, **2021**, *55*, 1-16. Academic Press.

[14] Richardson, J. O. Understanding chemical reactions beyond transition-state theory. *Chimia*, **2018**, *72* (5), 309-309.

[15] Bell, R. P. *The tunnel effect in chemistry*. **2013**, Springer.

[16] Andersson, S., Nyman, G., Arnaldsson, A., Manthe, U., & Jónsson, H. Comparison of quantum dynamics and quantum transition state theory estimates of the H+ CH4 reaction rate. *J. Phys. Chem A*, **2009**, *113* (16), 4468-4478.

[17] Pérez de Tudela, R., Suleimanov, Y. V., Richardson, J. O., Saez Rabanos, V., Green, W. H., & Aoiz, F. J. Stress test for quantum dynamics approximations: Deep tunneling in the muonium exchange reaction D+ HMu→ DMu+ H. *J. Phys. Chem. Lett.*, **2014**, *5* (23), 4219-4224.

[18] Richardson, J. O., & Althorpe, S. C. Ring-polymer molecular dynamics rate-theory in the deep-tunneling regime: Connection with semiclassical instanton theory. *J. Chem. Phys.*, **2009**, *131* (21).

[19] Goumans, T. P., & Kästner, J. Hydrogen-atom tunneling could contribute to H2 formation in space. *Angew. Chem. Int. Ed.*, **2010**, *49* (40), 7350-7352.

[20] Ess, D. H., Wheeler, S. E., Iafe, R. G., Xu, L., Celebi-Oelcuem, N., & Houk, K. N. Bifurcations on potential energy surfaces of organic reactions *Angew. Chem. Int. Ed.*, **2008**, *47* (40), 7592-7601.

[21] Rehbein, J., & Carpenter, B. K. Do we fully understand what controls chemical selectivity?. *Phys. Chem. Chem. Phys.*, **2011**, *13* (47), 20906-20922.

[22] Hare, S. R., & Tantillo, D. J. Post-transition state bifurcations gain momentum–current state of the field. *Pure Appl. Chem.,* **2017**, *89* (6), 679-698.

[23] Allen, K. D., Wegener, G., & White, R. H. Discovery of multiple modified F-430 coenzymes in methanogens and anaerobic methanotrophic archaea suggests possible new roles for F-430 in nature. *Appl. Environ. Microbiol.*, **2014**, *80* (20), 6403-6412.

[24] Richard, R. M., & Ball, D. W. Ab initio calculations on the thermodynamic properties of azaborospiropentanes. *J. Mol. Model,* **2008**, *14*, 871-878.

[25] Thauer, R. K. Biochemistry of methanogenesis: a tribute to Marjory Stephenson: 1998 Marjory Stephenson prize lecture. *Microbiology*, **1998**, *144* (9), 2377-2406.

[26] Grabarse, W., Mahlert, F., Duin, E.C., Goubeaud, M., Shima, S., Thauer, R.K., Lamzin, V., & Ermler, U., On the mechanism of biological methane formation: structural evidence for conformational changes in methyl-coenzyme M reductase upon substrate binding. *J. Mol. Biol.*, **2001**, *309* (1), 315-330.

[27] Goncearenco, A., & Berezovsky, I. N. Exploring the evolution of protein function in Archaea. *BMC Evol. Biol.*, **2012**, *12*, 1-14.

[28] Krüger, M., Meyerdierks, A., Glöckner, F.O., Amann, R., Widdel, F., Kube, M., Reinhardt, R., Kahnt, J., Böcher, R., Thauer, R.K., & Shima, S., A conspicuous nickel protein in microbial mats that oxidize methane anaerobically. *Nature*, **2003**, *426* (6968), 878-881.

[29] Shima, S., Krueger, M., Weinert, T., Demmer, U., Kahnt, J., Thauer, R. K., & Ermler, U. Structure of a methyl-coenzyme M reductase from Black Sea mats that oxidize methane anaerobically. *Nature*, **2012**, *481* (7379), 98-101.

[30] Scheller, S., Goenrich, M., Boecher, R., Thauer, R. K., & Jaun, B. The key nickel enzyme of methanogenesis catalyses the anaerobic oxidation of methane. *Nature*, **2010**, *465* (7298), 606-608.

[31] Shima, S., & Thauer, R. K. Methyl-coenzyme M reductase and the anaerobic oxidation of methane in methanotrophic Archaea. *Curr. Opin. Microbiol.*, **2005**, *8* (6), 643-648.

[32] Timmers, P. H., Welte, C. U., Koehorst, J. J., Plugge, C. M., Jetten, M. S., & Stams, A. J. Reverse methanogenesis and respiration in methanotrophic archaea. *Archaea*, **2017**, 1654237.

[33] Lemaire, O. N., & Wagner, T. A structural view of alkyl-coenzyme M reductases, the first step of alkane anaerobic oxidation catalyzed by archaea. *Biochemistry*, **2022**, *61* (10), 805-821.

[34] Thauer, R. K. Methyl (alkyl)-coenzyme M reductases: nickel F-430-containing enzymes involved in anaerobic methane formation and in anaerobic oxidation of methane or of short chain alkanes. *Biochemistry*, **2019**, *58* (52), 5198-5220.

[35] Moore, S.J., Sowa, S.T., Schuchardt, C., Deery, E., Lawrence, A.D., Ramos, J.V., Billig, S., Birkemeyer, C., Chivers, P.T., Howard, M.J., & Rigby, S.E., Elucidation of the biosynthesis of the methane catalyst coenzyme F430. *Nature*, **2017**, *543* (7643), 78-82.

[36] Lane, N. *The Vital Question: Why is Life the Way it is?,* Profile Books, **2016**.

[37] Ermler, U., Grabarse, W., Shima, S., Goubeaud, M., & Thauer, R. K. Crystal structure of methyl-coenzyme M reductase: the key enzyme of biological methane formation. *Science*, **1997**, *278* (5342), 1457-1462.

[38] Dey, M., Li, X., Kunz, R. C., & Ragsdale, S. W. Detection of organometallic and radical intermediates in the catalytic mechanism of methyl-coenzyme M reductase using the natural substrate methyl-coenzyme M and a coenzyme B substrate analogue. *Biochemistry*, **2010**, *49* (51), 10902-10911.

[39] Signor, L., Knuppe, C., Hug, R., Schweizer, B., Pfaltz, A., & Jaun, B. Methane formation by reaction of a methyl Thioether with a photo-excited nickel Thiolate—a process mimicking methanogenesis in Archaea. *Chem. – Eur. J.*, **2000**, *6* (19), 3508-3516.

[40] Grabarse, W., Mahlert, F., Duin, E.C., Goubeaud, M., Shima, S., Thauer, R.K., Lamzin, V. and Ermler, U., On the mechanism of biological methane formation: structural evidence for conformational changes in methyl-coenzyme M reductase upon substrate binding. *J. Mol. Biol.*, **2001**, *309* (1), 315-330.

[41] Duin, E. C., & McKee, M. L. A new mechanism for methane production from methyl-coenzyme M reductase as derived from density functional calculations. *J. Phys. Chem. B*, **2008**, *112* (8), 2466-2482.

[42] Pelmenschikov, V., Blomberg, M. R., Siegbahn, P. E., & Crabtree, R. H. A mechanism from quantum chemical studies for methane formation in methanogenesis. *J. Am. Chem. Soc.*, **2002**, *124* (15), 4039-4049.

[43] Pelmenschikov, V., & Siegbahn, P. E. Catalysis by methyl-coenzyme M reductase: a theoretical study for heterodisulfide product formation. *J. Biol. Inorg. Chem.*, **2003**, *8*, 653-662.

[44] Chen, S. L., Blomberg, M. R., & Siegbahn, P. E. How Is Methane Formed and Oxidized Reversibly When Catalyzed by Ni-Containing Methyl-Coenzyme M Reductase?. *Chem. – Eur. J.*, **2012**, *18* (20), 6309-6315.

[45] Patwardhan, A., Sarangi, R., Ginovska, B., Raugei, S., & Ragsdale, S. W. Nickel–sulfonate mode of substrate binding for forward and reverse reactions of methyl-SCoM reductase suggest a radical mechanism involving long-range electron transfer. *J. Am. Chem. Soc.*, **2021**, *143* (14), 5481-5496.

[46] Signor, L., Knuppe, C., Hug, R., Schweizer, B., Pfaltz, A., & Jaun, B. Methane formation by reaction of a methyl Thioether with a photo-excited nickel Thiolate—a process mimicking methanogenesis in Archaea. *Chem. – Eur. J.*, **2000**, *6* (19), 3508-3516.

[47] Grabarse, W., Mahlert, F., Duin, E.C., Goubeaud, M., Shima, S., Thauer, R.K., Lamzin, V., & Ermler, U., On the mechanism of biological methane formation: structural evidence for

conformational changes in methyl-coenzyme M reductase upon substrate binding. *J. Mol. Biol.*, **2001**, *309* (1), 315-330.

[48] Duin, E. C., & McKee, M. L. A new mechanism for methane production from methyl-coenzyme M reductase as derived from density functional calculations. *J. Phys. Chem. B*, **2008**, *112* (8), 2466-2482.

[49] Chen, S. L., Pelmenschikov, V., Blomberg, M. R., & Siegbahn, P. E. Is there a Ni-methyl intermediate in the mechanism of methyl-coenzyme M reductase?. *J. Am. Chem. Soc.*, **2009** *131* (29), 9912-9913.

[50] Chen, S. L., Blomberg, M. R., & Siegbahn, P. E. An investigation of possible competing mechanisms for Ni-containing methyl–coenzyme M reductase. *Phys. Chem. Chem. Phys.*, **2014**, *16* (27), 14029-14035.

[51] Wongnate, T., Sliwa, D., Ginovska, B., Smith, D., Wolf, M. W., Lehnert, N., Raugei, S., & Ragsdale, S. W. The radical mechanism of biological methane synthesis by methyl-coenzyme M reductase. *Science*, **2016**, *352* (6288), 953-958.

[52] Pasto, D. J., Garves, K., & Serve, M. P. Mechanism of solvolysis of phenacyl halides in various solvents. *J. Org. Chem.*, **1967**, *32* (3), 774-778.

[53] Hare, S. R., Li, A., & Tantillo, D. J. Post-transition state bifurcations induce dynamical detours in Pummerer-like reactions. *Chem. Sci.*, **2018**, *9* (48), 8937-8945.

[54] Hong, Y. J., & Tantillo, D. J. Quantum chemical dissection of the classic terpinyl/pinyl/bornyl/camphyl cation conundrum—the role of pyrophosphate in manipulating pathways to monoterpenes. *Org. Biomol. Chem.,* **2010**, *8* (20), 4589-4600.

[55] Noey, E. L., Wang, X., & Houk, K. N. Selective gold (I)-catalyzed formation of tetracyclic indolines: A single transition structure and bifurcations lead to multiple products. *J. Org. Chem.,* **2011**, *76* (9), 3477-3483.

[56] Hong, Y. J., & Tantillo, D. J. Biosynthetic consequences of multiple sequential post-transition-state bifurcations. *Nat. Chem.*, **2014**, *6* (2), 104-111.

[57] Singleton, D.A., Hang, C., Szymanski, M.J., Meyer, M.P., Leach, A.G., Kuwata, K.T., Chen, J.S., Greer, A., Foote, C.S., & Houk, K.N. Mechanism of ene reactions of singlet oxygen. A two-step no-intermediate mechanism. *J. Am. Chem. Soc.*, **2003**, *125* (5), 1319-1328.

[58] Bekele, T., Christian, C. F., Lipton, M. A., & Singleton, D. A. “Concerted” transition state, stepwise mechanism. Dynamics effects in C2-C6 enyne allene cyclizations. *J. Am. Chem. Soc.*, **2005**, *127* (25), 9216-9223.

[59] Litovitz, A. E., Keresztes, I., & Carpenter, B. K. Evidence for nonstatistical dynamics in the Wolff rearrangement of a carbene. *J. Am. Chem. Soc.*, **2008**, *130* (36), 12085-12094.

[60] Glowacki, D. R., Marsden, S. P., & Pilling, M. J. Significance of Nonstatistical Dynamics in Organic Reaction Mechanisms: Time-Dependent Stereoselectivity in Cyclopentyne− Alkene Cycloadditions. *J. Am. Chem. Soc.*, **2009**, *131* (39), 13896-13897.

[61] Wang, Z., Hirschi, J. S., & Singleton, D. A. Recrossing and dynamic matching effects on selectivity in a Diels-Alder reaction. *Angew. Chem., Int. Ed.,* **2009**, *48* (48), 9156-9159.

[62] Patel, A., Chen, Z., Yang, Z., Gutiérrez, O., Liu, H. W., Houk, K. N., & Singleton, D. A. Dynamically complex [6+ 4] and [4+ 2] cycloadditions in the biosynthesis of spinosyn A. *J. Am. Chem. Soc.*, **2016**, *138* (11), 3631-3634.

[63] Ang, S. J., Wang, W., Schwalbe-Koda, D., Axelrod, S., & Gómez-Bombarelli, R. Active learning accelerates ab initio molecular dynamics on reactive energy surfaces. *Chem*, **2021**, *7* (3), 738-751.

[64] Hare, S. R., Pemberton, R. P., & Tantillo, D. J. Navigating past a fork in the road: carbocation− π interactions can manipulate dynamic behavior of reactions facing post-transition-state bifurcations. *J. Am. Chem. Soc.*, **2017**, *139* (22), 7485-7493.

[65] Yang, Z., Dong, X., Yu, Y., Yu, P., Li, Y., Jamieson, C., & Houk, K. N. Relationships between product ratios in ambimodal pericyclic reactions and bond lengths in transition structures. *J. Am. Chem. Soc.*, **2018**, *140* (8), 3061-3067.

[66] Li, B., Li, Y., Dang, Y., & Houk, K. N. Post-transition state bifurcation in iron-catalyzed arene aminations. *ACS Catal.*, **2021**, *11* (12), 6816-6824.

[67] Zhang, H., Novak, A. J., Jamieson, C. S., Xue, X. S., Chen, S., Trauner, D., & Houk, K. N. Computational exploration of the mechanism of critical steps in the biomimetic synthesis of preuisolactone A, and discovery of new ambimodal (5+ 2)/(4+ 2) cycloadditions. *J. Am. Chem. Soc.*, **2021**, *143* (17), 6601-6608.

[68] Jamieson, C. S., Sengupta, A., & Houk, K. N. Cycloadditions of cyclopentadiene and cycloheptatriene with tropones: All endo-[6+ 4] cycloadditions are ambimodal. *J. Am. Chem. Soc.*, **2021**, *143* (10), 3918-3926.

[69] Peterson, T. H., & Carpenter, B. K. Estimation of dynamic effects on product ratios by vectorial decomposition of a reaction coordinate. Application to thermal nitrogen loss from bicyclic azo compounds. *J. Am. Chem. Soc.*, **1992**, *114* (2), 766-767.

[70] Lee, S., & Goodman, J. M. Rapid route-finding for bifurcating organic reactions. *J. Am. Chem. Soc.*, **2020**, *142* (20), 9210-9219.

[71] Lee, S., & Goodman, J. M. VRAI-selectivity: calculation of selectivity beyond transition state theory. *Org. Biomol. Chem*., **2021**, *19* (17), 3940-3947.

[72] Russell, J. B. General Chemistry, *McGraw-Hill International Book Company*, **1980**.

[73] Jensen, F. *Introduction to Computational Chemistry*, John Wiley & Sons Ltd., Baffins Lane, Chichester, West Sussex PO19 1UD, England, **1999**.

[74] Frisch, M. J., Trucks, G. W., Schlegel, H. B., Scuseria, G. E., Robb, M. A., Cheeseman, J. R., Montgomery, J. A., Jr., Vreven, T., Kudin, K. N., Burant, J. C., Millam, J. M., Iyengar, S. S., Tomasi, J., Barone, V., Mennucci, B., Cossi, M., Scalmani, G., Rega, N., Petersson, G. A., Nakatsuji, H., Hada, M., Ehara, M., Toyota, K., Fukuda, R., Hasegawa, J., Ishida, M., Nakajima, T., Honda, Y., Kitao, O., Nakai, H., Klene, M., Li, X., Knox, J. E., Hratchian, H. P., Cross, J. B., Bakken, V., Adamo, C., Jaramillo, J., Gomperts, R., Stratmann, R. E., Yazyev, O., Austin, A. J., Cammi, R., Pomelli, C., Ochterski, J. W., Ayala, P. Y., Morokuma, K., Voth, G. A., Salvador, P. J., Dannenberg, J., Zakrzewski, V. G., Dapprich, S., Daniels, A. D., Strain, M. C., Farkas, O., Malick, D. K., Rabuck, A. D., Raghavachari, K., Foresman, J. B., Ortiz, J. V., Cui, Q., Baboul, A. G., Clifford, S., Cioslowski, J., Stefanov, B. B., Liu, G., Liashenko, A., Piskorz, P., Komaromi, I., Martin, R. L., Fox, D. J., Keith, T., Al- Laham, M. A., Peng, C. Y., Nanayakkara, A., Challacombe, M., Gill, P. M. W., Johnson, B., Chen, W., Wong, M. W., Gonzalez, C., and Pople, J. A. *Gaussian 03*, *revision D.02*; Gaussian, Inc., Pittsburgh, PA, 2003; (b) Frisch, M. J., Trucks, G. W., Schlegel, H. B., Scuseria, G. E., Robb, M. A., Cheeseman, J. R., Scalmani, G., Barone, V., Mennucci, B., Petersson, G. A., Nakatsuji, H., Caricato, M., Li, X., Hratchian, H. P., Izmaylov, A. F., Bloino, J., Zheng, G., Sonnenberg, J. L., Hada, M., Ehara, M., Toyota, K., Fukuda, R., Hasegawa, J., Ishida, M., Nakajima, T., Honda, Y., Kitao, O., Nakai, H., Vreven, T., Montgomery, J. A., Peralta, Jr., J. E., Ogliaro, F., Bearpark, M., Heyd, J. J., Brothers, E., Kudin, K. N., Staroverov, V. N., Kobayashi, R., Normand, J., Raghavachari, K., Rendell, A., Burant, J. C., Iyengar, S. S., Tomasi, J., Cossi, M., Rega, N., Millam, J. M., Klene, M., Knox, J. E., Cross J. B., Bakken, V., Adamo, C., Jaramillo, J., Gomperts, R., Stratmann, R. E., Yazyev, O., Austin, A. J., Cammi, R., Pomelli, C., Ochterski,

J. W., Martin, R. L., Morokuma, K., Zakrzewski, V. G., Voth, G. A., Salvador, P., Dannenberg, J. J., Dapprich, S., Daniels, A. D., Farkas, Ö., Foresman, J. B., Ortiz, J. V., Cioslowski, J., & Fox, D. J. *Gaussian 09*, *Revision D.01*, Gaussian, Inc., Wallingford CT, **2009**.

[75] Pople, J. A. Quantum chemical models (Nobel lecture). *Angew. Chem., Int. Ed.*, **1999**, *38* (13-14), 1894-1902.

[76] Kohn, W. Nobel Lecture: Electronic structure of matter—wave functions and density functionals. *Reviews of Modern Physics*, **1999**, *71* (5), 1253.

[77] Karplus, M. Development of multiscale models for complex chemical systems: from H+ H2 to biomolecules (Nobel lecture). *Angew. Chem., Int. Ed.*, **2014**, *53* (38), 9992-10005.

[78] Karplus, M., Levitt, M., and Warshel, A. The Nobel Prize in Chemistry 2013. *Nobel Media AB 2014*, **2013**.

[79] Lewars, E. *Computational chemistry: Introduction to the theory and applications of molecular and quantum mechanics*, Springer (India) Pvt. Ltd., New Delhi, 2nd Edition, **2008**.

[80] Koch, W. and Holthausen, M. C. *A Chemist's Guide to Density Functional Theory*, Wiley-VCH, Weinheim, **2000**.

[81] Parr, R. G., & Yang, W. *Density functional theory of Atoms and Molecules*, Oxford University Press, Oxford, New York, **1989**.

[82] Hohenberg, P., & Kohn, W. Inhomogeneous electron gas. *Physical Review*, **1964**, *136* (3B), B864.

[83] Kohn, W. and Sham, L. J. Self-consistent equations including exchange and correlation effects. *Physical Review*, **1965**, *140* (4A), A1133.

[84] Kohn, W., Becke, A. D., & Parr, R. G. Density functional theory of electronic structure. *J. Phys. Chem.*, **1996**, *100* (31), 12974-12980.

[85] Baerends, E. J., & Gritsenko, O. V. A quantum chemical view of density functional theory. *J. Phys. Chem. A*, **1997,** *101* (30), 5383-5403.

[86] Ghosh, S. K. Density Functional Theory and Materials Modelling at Atomistic Length Scales. *Int. J. Mol. Sci.*, **2002**, *3* (4), 260-275.

[87] Geerlings, P., De Proft, F., & Langenaeker, W. Conceptual density functional theory. *Chem. Rev.*, **2003**, *103* (5), 1793-1874.

[88] Bartolotti, L. J., & Flurchick, K. An introduction to density functional theory. *Reviews in Computational Chemistry*, **1996**, *7*, 187-260.

[89] St-Amant, A. Density functional methods in biomolecular modeling. *Reviews in Computational Chemistry*, **1996**, 7, 217.

[90] ) Ziegler, T. Approximate density functional theory as a practical tool in molecular energetics and dynamics. *Chem. Rev.*, **1991**, *91* (5), 651-667.

[91] Slater, J. C. A simplification of the Hartree-Fock method. *Physical Review*, **1951**, *81* (3), 385.

[92] Becke, A. D. Density-functional exchange-energy approximation with correct asymptotic behavior. *Physical Review A*, **1988**, *38* (6), 3098-3100.

[93] Gill, P. M. A new gradient-corrected exchange functional. *Molecular Physics*, **1996**, *89* (2), 433-445.

[94] Adamo, C., & Barone, V. Implementation and validation of the Lacks-Gordon exchange functional in conventional density functional and adiabatic connection methods. *J. Comput. Chem.*, **1998**, *19* (4), 418-429.

[95] Lee, C., Yang, W., & Parr, R. G. Development of the Colle-Salvetti correlation-energy formula into a functional of the electron density. *Physical Review B*, **1988**, *37* (2), 785-789.

[96] Perdew, J. P. Density-functional approximation for the correlation energy of the inhomogeneous electron gas. *Physical Review B*, **1986**, *33* (12), 8822-8824.

[97] Perdew, J. P., & Yue, W. Accurate and simple density functional for the electronic exchange energy: Generalized gradient approximation. *Physical Review B*, **1986**, *33* (12), 8800.

[98] Perdew, J. P., Burke, K., & Wang, Y. Generalized gradient approximation for the exchange-correlation hole of a many-electron system. *Physical Review B*, **1996**, *54* (23),16533-16539.

[99] Zhao, Y., & Truhlar, D. G. The M06 suite of density functionals for main group thermochemistry, thermochemical kinetics, noncovalent interactions, excited states, and transition elements: two new functionals and systematic testing of four M06-class functionals and 12 other functionals. *Theor. Chem. Acc.,* **2008**, *120* (1-3), 215–241.

[100] Stephens, P. J., Devlin, F. J., Chabalowski, C. F. N., & Frisch, M. J. Ab initio calculation of vibrational absorption and circular dichroism spectra using density functional force fields. *J. Phys. Chem.*, **1994**, *98* (45), 11623-11627.

[101] Slater, J. C. Atomic shielding constants. *Physical Review*, **1930**, *36* (1), 57-64.

[102] Boys, S. F. Electronic wave functions-I. A general method of calculation for the stationary states of any molecular system. *Proceedings of the Royal Society A*, **1950**, *200* (1063), 542-554.

[103] Hehre, W. J., Stewart, R. F., & Pople, J. A. Self-consistent molecular-orbital methods. I. Use of gaussian expansions of Slater-type atomic orbitals. *J. Chem. Phys.*, **1969**, *51* (6), 2657-2664.

[104] Binkley, J. S., Pople, J. A., & Hehre, W. J. Self-consistent molecular orbital methods. 21. Small split-valence basis sets for first-row elements. *J. Am. Chem. Soc.*, **1980**, *102* (3), 939-947.

[105] Ditchfield, R. H. W. J., Hehre, W. J., & Pople, J. A. Self-consistent molecular-orbital methods. IX. An extended Gaussian-type basis for molecular-orbital studies of organic molecules. *J. Chem. Phys.*, **1971**, *54* (2), 724-728.

[106] McLean, A. D., & Chandler, G. S. Contracted Gaussian basis sets for molecular calculations. I. Second row atoms, Z= 11–18. *J. Chem. Phys.*, **1980**, *72* (10), 5639-5648.

[107] Krishnan, R. B. J. S., Binkley, J. S., Seeger, R., & Pople, J. A. Self-consistent molecular orbital methods. XX. A basis set for correlated wave functions. *J. Chem. Phys.*, **1980**, *72* (1), 650-654.

[108] Petersson, A., Bennett, A., Tensfeldt, T. G., Al-Laham, M. A., Shirley, W. A., & Mantzaris, J. A complete basis set model chemistry. I. The total energies of closed-shell atoms and hydrides of the first-row atoms. *J. Chem. Phys.,* **1998**, *89* (4), 2193-2218.

[109] Petersson, G. A., & Al-Laham, M. A. A complete basis set model chemistry. II. Open-shell systems and the total energies of the first-row atoms. *J. Chem. Phys.,* **1991**, *94* (9), 6081-6090.

[110] Frenking, G., Antes, I., Böhme, M., Dapprich, S., Ehlers, A. W., Jonas, V., Neuhaus, A., Otto, M., Stegmann, R., Veldkamp, A., & Vyboishchikov, S. F. Pseudopotential calculations of transition metal compounds: scope and limitations. *Reviews in Computational Chemistry*, **2007**, *8*, 63-144.

[111] Hay, P. J. & Wadt, W. R. Ab initio effective core potentials for molecular calculations. Potentials for the transition metal atoms Sc to Hg. *J. Chem. Phys.,* **1985**, *82* (1), 270-283.

[112] Wadt, W. R. & Hay, P. J. Ab initio effective core potentials for molecular calculations. Potentials for main group elements Na to Bi. *J. Chem. Phys.,* **1985**, *82* (1), 284-298.

[113] Hay, P. J. and Wadt, W. R. Ab initio effective core potentials for molecular calculations. Potentials for K to Au including the outermost core orbitals *J. Chem. Phys.,* **1985,** *82* (1), 299-310.

[114] Fuentealba, P., Preuss, H., Stoll, H., & Von Szentpály, L. A proper account of core-polarization with pseudopotentials: single valence-electron alkali compounds. *Chem. Phys. Lett.*, **1982**, *89* (5), 418-422.

[115] Von Szentpály, L., Fuentealba, P., Preuss, H., & Stoll, H. Pseudopotential calculations on Rb+ 2, Cs+ 2, RbH+, CsH+ and the mixed alkali dimer ions. . *Chem. Phys. Lett.*, **1982**, *93* (6), 555-559.

[116] Fuentealba, P., Stoll, H., Von Szentpaly, L., Schwerdtfeger, P., & Preuss, H. On the reliability of semi-empirical pseudopotentials: simulation of Hartree-Fock and Dirac-Fock results. *Journal of Physics B: Atomic and Molecular Physics*, **1983**, *16* (11), L323.

[117] Cossi, M., Rega, N., Scalmani, G., & Barone, V. Energies, structures, and electronic properties of molecules in solution with the C-PCM solvation model. *J. Comput. Chem.,* **2003**, *24* (6), 669-681.

[118] Weigend, F., & Ahlrichs, R. Balanced basis sets of split valence, triple zeta valence and quadruple zeta valence quality for H to Rn: Design and assessment of accuracy. *Phys. Chem. Chem. Phys.,* **2005**, *7* (18), 3297-3305.

[119] Weigend, F. Accurate Coulomb-fitting basis sets for H to Rn *Phys. Chem. Chem. Phys.*, **2006**, *8* (9), 1057-1065.

[120] Francl, M. M., Pietro, W. J., Hehre, W. J., Binkley, J. S., Gordon, M. S., DeFrees, D. J., & Pople, J. A. Self-consistent molecular orbital methods. XXIII. A polarization-type basis set for second-row elements. *J. Chem. Phys.,* **1982**, *77* (7), 3654-3665.

[121] Wu, J., & Chen, S. L. Handling methane: a Ni (i) F 430-like cofactor derived from VB 12 is active in methyl-coenzyme M reductase. *Chem. Comm.,* **2021**, *57* (4), 476-479.

[122] Grimme, S., Antony, J., Ehrlich, S., & Krieg, H. A consistent and accurate ab initio parametrization of density functional dispersion correction (DFT-D) for the 94 elements H-Pu. *J. Chem. Phys.*, **2010**, *132* (15), 154104.

[123] Biegler-könig, F. W., Bader, R. F., & Tang, T. H. Calculation of the average properties of atoms in molecules. II. *J. Comput. Chem*., **1982**, *3* (3), 317-328.

[124] Kelly, C. P., Cramer, C. J., & Truhlar, D. G. Aqueous solvation free energies of ions and ion− water clusters based on an accurate value for the absolute aqueous solvation free energy of the proton. *J. Phys. Chem. B*, **2006**, *110* (32), 16066-16081.

[125] Friedle, S., Reisner, E., & Lippard, S. J. Current challenges of modeling diiron enzyme active sites for dioxygen activation by biomimetic synthetic complexes. *Chem. Soc. Rev.*, **2010**, *39* (8), 2768-2779.

[126] Bo, C., & Maseras, F. QM/MM methods in inorganic chemistry. *Dalton Transactions*, **2008**, *22*, 2911-2919.

[127] Balasubramanian, K. Relativistic quantum chemical and molecular dynamics techniques for medicinal chemistry of bioinorganic compounds. *In Biophysical and Computational Tools in Drug Discovery* (**2021**, 133-193*). Cham: Springer International Publishing*.

[128] Kirchner, B., Wennmohs, F., Ye, S., & Neese, F. Theoretical bioinorganic chemistry: the electronic structure makes a difference. *Current opinion in chemical biology*, **2007**, *11* (2), 134-141.

[129] Borowski, T., Quesne, M., & Szaleniec, M. QM and QM/MM methods compared: Case studies on reaction mechanisms of metalloenzymes. *Advances in Protein Chemistry and Structural Biology*, **2015**, *100*, 187-224.

[130] Vidossich, P., & Magistrato, A. QM/MM molecular dynamics studies of metal binding proteins. *Biomolecules*, **2014**, *4* (3), 616-645.

[131] van der Kamp, M. W., & Mulholland, A. J. Combined quantum mechanics/molecular mechanics (QM/MM) methods in computational enzymology. *Biochemistry*, **2013**, *52* (16), 2708-2728.

[132] Schulz, C. E., Castillo, R. G., Pantazis, D. A., DeBeer, S., & Neese, F. Structure–spectroscopy correlations for intermediate Q of soluble methane monooxygenase: insights from QM/MM calculations. *J. Am. Chem. Soc.*, **2021**, *143* (17), 6560-6577.

[133] Birrell, J.A., Pelmenschikov, V., Mishra, N., Wang, H., Yoda, Y., Tamasaku, K., Rauchfuss, T.B., Cramer, S.P., Lubitz, W., & DeBeer, S., Spectroscopic and computational evidence that [FeFe] hydrogenases operate exclusively with CO-bridged intermediates. *J. Am. Chem. Soc.*, **2019**, *142* (1), 222-232.

[134] Pelmenschikov, V., Birrell, J.A., Gee, L.B., Richers, C.P., Reijerse, E.J., Wang, H., Arragain, S., Mishra, N., Yoda, Y., Matsuura, H., & Li, L., Vibrational perturbation of the [FeFe] hydrogenase H-cluster revealed by 13C2H-ADT labeling. *J. Am. Chem. Soc.*, **2021**, *143* (22), 8237-8243.

[135] Tai, H., Hirota, S., & Stripp, S. T. Proton transfer mechanisms in bimetallic hydrogenases. *Acc. Chem. Res.*, **2020**, *54* (1), 232-241.

[136] Wigner, E. The transition state method. *Trans. Faraday. Soc.*, **1938**, *34*, 29-41.

[137] Horiuti, J. On the statistical mechanical treatment of the absolute rate of chemical reaction. *Bull. Chem. Soc. Jpn*., **1938**, *13* (1), 210-216.

[138] Bligaard, T., & Nørskov, J. K. (2008). Heterogeneous catalysis. *In Chemical bonding at surfaces and interfaces*, **2008**, 255-321. *Elsevier*.

[139] Arrhenius, S. Über die Reaktionsgeschwindigkeit bei der Inversion von Rohrzucker durch Säuren. *Z. Phys. Chem*., **1889**, *4* (1), 226-248.

[140] Arrhenius, S. Über die Dissociationswärme und den Einfluss der Temperatur auf den Dissociationsgrad der Elektrolyte. *Z. Phys. Chem.*, **1889**, *4* (1), 96-116.

[141] Laidler, K. J. The development of the Arrhenius equation. *J. Chem. Educ.*, **1984**, *61* (6), 494.

[142] Anslyn, E. V., & Dougherty, D. A. *Modern physical organic chemistry*, **2006**, 365-373.

[143] Maldonado-Domínguez, M., Bím, D., Fučík, R., Čurík, R., & Srnec, M. Reactive mode composition factor analysis of transition states: The case of coupled electron–proton transfers. *Phys. Chem. Chem. Phys.*, **2019**, *21* (45), 24912-24918.

[144] Anslyn, E. V., & Dougherty, D. A. *Modern physical organic chemistry*. University science books, Sausalito, CA, **2006**.

[145] Bao, J. L., & Truhlar, D. G. Variational transition state theory: theoretical framework and recent developments. *Chem. Soc. Rev.*, **2017**, *46* (24), 7548-7596.

[146] Xue, X. S., Jamieson, C. S., Garcia-Borràs, M., Dong, X., Yang, Z., & Houk, K. N. Ambimodal trispericyclic transition state and dynamic control of periselectivity. *J. Am. Chem. Soc.*, **2019**, *141* (3), 1217-1221.

[147] Liu, C. Y., & Ding, S. T. Cycloadditions of electron-deficient 8, 8-disubstituted heptafulvenes to electron-rich 6, 6-disubstituted fulvenes. *J. Org. Chem.,* **1992**, *57* (16), 4539-4544.

[148] Liu, C. Y., Ding, S. T., Chen, S. Y., You, C. Y., & Shie, H. Y. Steric effects in the cycloaddition reactions of electron-deficient unsymmetrically 8, 8-disubstituted 8-cyano-8-(methoxycarbonyl) heptafulvene with electron-rich 6, 6-diphenyl-and 6, 6-dimethylfulvenes. *J. Org. Chem.,* **1993**, *58* (6), 1628-1630.

[149] Sweeny, B. C., Pan, H., Kassem, A., Sawyer, J. C., Ard, S. G., Shuman, N. S., & Meuwly, M. Thermal activation of methane by MgO+: temperature dependent kinetics, reactive molecular dynamics simulations and statistical modeling. *Phys. Chem. Chem. Phys*., **2020**, *22* (16), 8913-8923.

[150] Murakami, T., Ibuki, S., Hashimoto, Y., Kikuma, Y., & Takayanagi, T. Dynamics study of the post-transition-state-bifurcation process of the (HCOOH) H+→ CO+ H 3 O+/HCO++ H 2 O dissociation: application of machine-learning techniques. *Phys. Chem. Chem. Phys*., **2023**, *25* (20), 14016-14027.

[151] Hare, S. R., & Tantillo, D. J. (2017). Cryptic post-transition state bifurcations that reduce the efficiency of lactone-forming Rh-carbenoid C–H insertions. *Chem. Sci.*, **2017**, *8* (2), 1442-1449.

[152] Yamamoto, Y., Hasegawa, H., & Yamataka, H. Dynamic path bifurcation in the Beckmann reaction: support from kinetic analyses. *J. Org. Chem.,* **2011**, *76* (11), 4652-4660.

[153] Yamataka, H., Sato, M., Hasegawa, H., & Ammal, S. C. Dynamic path bifurcation for the Beckmann reaction: observation and implication. *Faraday Discussions*, **2010**, *145*, 327-340.

[154] Carpenter, B. K., Harvey, J. N., & Glowacki, D. R. Prediction of enhanced solvent-induced enantioselectivity for a ring opening with a bifurcating reaction path. *Phys. Chem. Chem. Phys*., **2015**, *17* (13), 8372-8381.

[155] Lei, Y., Wu, H., Zheng, X., Zhai, G., & Zhu, C. Photo-induced 1, 3-cyclohexadiene ring opening reaction: Ab initio on-the-fly nonadiabatic molecular dynamics simulation *J. Photochem. Photobiol.*, A., **2016**, *317*, 39-49.

[156] Maeda, S., Harabuchi, Y., Ono, Y., Taketsugu, T., & Morokuma, K. (2015). Intrinsic reaction coordinate: Calculation, bifurcation, and automated search. *Int. J. Quantum Chem.,* **2015**, *115* (5), 258-269.

[157] Katori, T., Itoh, S., Sato, M., & Yamataka, H. Reaction pathways and possible path bifurcation for the Schmidt reaction. *J. Am. Chem. Soc.*, **2010**, *132* (10), 3413-3422.

[158] Akimoto, R., Tokugawa, T., Yamamoto, Y., & Yamataka, H.. Reaction Pathway and Rate-Determining Step of the Schmidt Rearrangement/Fragmentation: A Kinetic Study. *J. Org. Chem.,* **2012**, *77* (8), 4073-4078.

[159] Hanessian, S., & Compain, P. Lewis acid promoted cyclocondensations of α-ketophosphonoenoates with dienes—from Diels–Alder to hetero Diels–Alder reactions. *Tetrahedron*, **2002**, *58* (32), 6521-6529.

[160] Denmark, S. E., Kesler, B. S., & Moon, Y. C. Inter-and intramolecular [4+ 2] cycloadditions of nitroalkenes with olefins. 2-Nitrostyrenes. *J. Org. Chem.*, **1992**, *57* (18), 4912-4924.

[161] Çelebi-Ölçüm, N., Ess, D. H., Aviyente, V., & Houk, K. N. Lewis Acid Ca

talysis Alters the Shapes and Products of Bis-Pericyclic Diels− Alder Transition States. *J. Am. Chem. Soc.*, **2007**, *129* (15), 4528-4529.

[162] Limanto, J., Khuong, K. S., Houk, K. N., & Snapper, M. L. Intramolecular cycloadditions of cyclobutadiene with dienes: Experimental and computational studies of the competing (2+ 2) and (4+ 2) modes of reaction. *J. Am. Chem. Soc.*, **2003**, *125* (52), 16310-16321.

[163] Harmata, M., & Gomes, M. G., Intermolecular [4+ 2] cycloadditions of a reactive cyclopentadienone. *Eur. J. Org. Chem*., **2006**, 2273–2277.

[164] Thomas, J. B., Waas, J. R., Harmata, M., & Singleton, D. A. Control elements in dynamically determined selectivity on a bifurcating surface *J. Am. Chem. Soc.*, **2008**, *130* (44), 14544-14555.

[165] Schmittel, M., Keller, M., Kiau, S., & Strittmatter, M. A Surprising Switch from the Myers–Saito Cyclization to a Novel Biradical Cyclization in Enyne–Allenes: Formal Diels–Alder and Ene Reactions with High Synthetic Potential. *Chem.–Eur. J.,* **1997**, *3* (5), 807-816.

[166] Yamabe, S., Dai, T., Minato, T., Machiguchi, T., & Hasegawa, T. Ketene Is a Dienophile for [4+ 2](Diels− Alder) Reactions across Its CO Bond1. *J. Am. Chem. Soc.,* **1996**, *118* (27), 6518-6519.

[167] Yu, P., Chen, T. Q., Yang, Z., He, C. Q., Patel, A., Lam, Y. H., & Houk, K. N. Mechanisms and origins of periselectivity of the ambimodal [6+ 4] cycloadditions of tropone to dimethylfulvene. *J. Am. Chem. Soc.,* **2017**, *139* (24), 8251-8258.

[168] Chen, S., Yu, P., & Houk, K. N. Ambimodal dipolar/Diels–Alder cycloaddition transition states involving proton transfers. *J. Am. Chem. Soc.,* **2018**, *140* (51), 18124-18131.

[169] Ohashi, M., Liu, F., Hai, Y., Chen, M., Tang, M. C., Yang, Z., & Tang, Y. SAM-dependent enzyme-catalysed pericyclic reactions in natural product biosynthesis. *Nature*, **2017**, *549* (7673), 502-506.

[170] Villar Lopez, R., Faza, O. N., & Silva Lopez, C. Dynamic effects responsible for high selectivity in a [3, 3] sigmatropic rearrangement featuring a bispericyclic transition state. *J. Org. Chem.,* **2017**, *82* (9), 4758-4765.

[171] Ye, L., Wang, Y., Aue, D. H., & Zhang, L. Experimental and computational evidence for gold vinylidenes: Generation from terminal alkynes via a bifurcation pathway and facile C–H insertions. *J. Am. Chem. Soc.,* **2012**, *134* (1), 31-34.

[172] Campos, R. B., & Tantillo, D. J. Designing reactions with post-transition-state bifurcations: asynchronous nitrene insertions into C–C σ bonds. *Chem*, **2019**, 5 (1), 227-236.

[173] Mandal, N., & Datta, A. Dynamical Effects along the Bifurcation Pathway Control Semibullvalene Formation in Deazetization Reactions. *J. Phys. Chem. B,* **2018**, *122* (3), 1239-1244.

[174] Major, D. T., & Weitman, M. Electrostatically Guided Dynamics The Root of Fidelity in a Promiscuous Terpene Synthase?. *J. Am. Chem. Soc.,* **2012**, *134* (47), 19454-19462.

[175] Bogle, X. S., & Singleton, D. A. Dynamic origin of the stereoselectivity of a nucleophilic substitution reaction. *Org. Lett.*, **2012**, *14* (10), 2528-2531.

[176] Itoh, S., Yoshimura, N., Sato, M., & Yamataka, H. Computational study on the reaction pathway of α-bromoacetophenones with hydroxide ion: possible path bifurcation in the addition/substitution mechanism. *J. Org. Chem.*, **2011**, *76* (20), 8294-8299.

[177] Merrer, D. C., & Rablen, P. R. Dichlorocarbene addition to cyclopropenes: A computational study. *J. Org. Chem.*, **2005**, *70* (5), 1630-1635.

[178] Khrapunovich, M., Zelenova, E., Seu, L., Sabo, A. N., Flaherty, A., & Merrer, D. C. Regioselectivity and mechanism of dihalocarbene addition to benzocyclopropene. *J. Org. Chem.,* **2007**, *72* (20), 7574-7580.

[179] Noey, E.L., Yang, Z., Li, Y., Yu, H., Richey, R.N., Merritt, J.M., Kjell, D.P., & Houk, K.N., 2017. Origins of regioselectivity in the Fischer indole synthesis of a selective androgen receptor modulator. *J. Org. Chem.*, **2017**, *82* (11), 5904-5909.

[180] Kim, H. J., Ruszczycky, M. W., Choi, S. H., Liu, Y. N., & Liu, H. W. Enzyme-catalysed [4+ 2] cycloaddition is a key step in the biosynthesis of spinosyn A. Nature, **2011**, *473* (7345), 109-112.

# 10. List of publications:

**The thesis is based on following publications:**

**Paper I**

**Bifurcating reactions: distribution of products from energy distribution in a shared reactive mode.**

**P Bharadwaz**, M Maldonado-Domínguez, M Srnec

*Chemical Science*, **2021**, *12* (38), 12682-12694.

**Paper II**

**Reactivity Factors in Catalytic Methanogenesis and Their Tuning upon Coenzyme F430 Biosynthesis.**

**P Bharadwaz**, M Maldonado-Domínguez, J Chalupský, M Srnec

*Journal of the American Chemical Society* **2023**, *145* (16), 9039-9051.

**Other publications:**

1. **Elucidation of factors shaping reactivity of 5'-deoxyadenosyl - a prominent organic radical in biology.**

Z Wojdyla, M Maldonado-Domínguez, **P Bharadwaz**, Martin Culka, M Srnec

*(Submitted)*

2. **Computational investigation on the effect of the peptidomimetic inhibitors (NPT100-18Aand NPT200-11) on the α-synuclein and lipid membrane interactions.**

D. Das*, **P. Bharadwaz***, V. S. Mattaparthi

*Journal of Biomolecular Structure and Dynamics*, **2023**, 1-12.

3. **Activation of small molecules by cyclic alkyl amino silylenes (CAASis) and germylenes (CAAGes): a theoretical study.**

B. Ghosh*, **P. Bhardawaz***, N. Sarkar, A. K. Phukan

*Dalton Transactions*, **2020**, *49* (39), 13760-13772.

4. **Introducing N-Heterocyclic Borylenes: Theoretical Prediction of Stable, Neutral, Monomeric Boron (I) Carbenoids.**
**P. Bhardawaz,** A. K. Phukan
*Inorganic Chemistry*, **2019**, *58* (9), 5428-5432.

5. **Metal-Free Activation of Enthalpically Strong Bonds: Unraveling the Potential of Hitherto Unexplored Singlet Carbenes.**
**P. Bhardawaz,** R. D. Dewhurst, A. K. Phukan
*Advanced Synthesis & Catalysis*, **2018**, *360* (23), 4543-4561.

6**. Electronic and ligand properties of skeletally substituted cyclic (alkyl)(amino) carbenes (CAACs) and their reactivity towards small molecule activation: a theoretical study.**
**P. Bhardawaz,** P. Chetia, A. K. Phukan
*Chemistry–A European Journal*, **2017**, *23* (41), 9926-9936.

7. **Annulated boron substituted N-heterocyclic carbenes: theoretical prediction of highly electrophilic carbenes.**
**P. Bhardawaz,** B. Borthakur, A. K. Phukan
*Dalton Transactions*, **2015**, *44* (42), 18656-18664.